# Turbulent boundary layer control utilizing the Lorentz force

Timothy W. Berger, John Kim,[a] Changhoon Lee,[b] and Junwoo Lim
*Department of Mechanical & Aerospace Engineering, University of California, Los Angeles, California 90095*

(Received 18 May 1999; accepted 19 November 1999)

Direct numerical simulations (DNS) of a turbulent channel flow at low Reynolds number ($Re_\tau = 100,200,400$, where $Re_\tau$ is the Reynolds number based on the wall-shear velocity and channel half-width) are carried out to examine the effectiveness of using the Lorentz force to reduce skin friction. The Lorentz force is created by embedding electrodes and permanent magnets in the flat surface over which the flow passes. Both open-loop and closed-loop control schemes are examined. For open-loop control, both temporally and spatially oscillating Lorentz forces in the near-wall region are tested. It is found that skin-friction drag can be reduced by approximately 40% if a temporally oscillating spanwise Lorentz force is applied to a $Re_\tau = 100$ channel flow. However, the power to generate the required Lorentz force is an order of magnitude larger than the power saved due to the reduced drag. Simulations were carried out at higher Reynolds numbers ($Re_\tau = 200,400$) to determine whether efficiency, defined as the ratio of the power saved to the power used, improves with increasing Reynolds number. We found that the efficiency decreases with increasing Reynolds number. An idealized wall–normal Lorentz force is effected by detecting the near-wall turbulent events responsible for high-skin friction. It is found that the drag can be significantly reduced with a greater efficiency than that produced by the spanwise open-loop control approach. This result suggests that, when employed with a closed-loop control scheme, the Lorentz force might result in a net decrease of power required to propel objects through viscous conducting fluids.  [S1070-6631(00)02203-0]

## I. INTRODUCTION

The possibilities for flow control afforded by the Lorentz force generated when an electrically conducting fluid flows through an electromagnetic field has been recognized for some time.[1–3] Exploiting this mechanism to reduce viscous drag has also been proposed. Most existing work,[1–5] however, involves imposing the Lorentz force along the flow direction, thus creating an additional streamwise acceleration in the flow direction. To the best of our knowledge, no successful experimental verification of a net drag reduction using this approach has yet been reported. Furthermore, the current understanding of the effect of the Lorentz force on turbulence dynamics is very limited, with many basic questions still open. It is our goal of this study to obtain a deeper understanding of the fundamental physics of turbulent boundary layers subjected to electromagnetic body forces.

Gailitis and Lielausis[2] appear to have been the first to propose use of the Lorentz force for flow control. In their analyses, a streamwise Lorentz force was applied to a laminar boundary layer in order to increase the thrust force and delay transition to turbulence of the flow over submerged vehicles by preventing the thickness of the laminar boundary layer profile from increasing. Tsinober and Shtern[3] showed clearly that a Blasius boundary layer profile becomes more stable when the Lorentz force is applied to the flow, created by an alternating array of electrodes and magnets (similar to Fig. 1, see Sec. IV for further detail). Lin[6] found that the critical Reynolds number for the modified profile is on the order of approximately $4\times10^4$, which is lower than that for a Blasius flow. However, the new profile does not grow in the flow direction as rapidly as the Blasius flow does and, hence, is more stable.

The Princeton group (e.g., Nosenchuck and Brown[7] and Nosenchuck[8]) explored the possibility of achieving viscous drag reduction in turbulent boundary layers with the Lorentz force. In these experiments, the Lorentz force was created along the wall–normal (perpendicular to the flow) direction. The Lorentz force interacted with the near-wall turbulence structures responsible for turbulence production. This approach was in contrast to earlier attempts, in which the Lorentz force was used *directly* to provide an additional acceleration in the flow direction, thereby modifying the mean flow. In the Princeton group experiment, the Lorentz force was used *indirectly*, to influence the relevant turbulence structures believed to be most responsible for skin friction in turbulent boundary layers. Although some of their results indicate that turbulence is significantly affected by the wall–normal Lorentz force, none of their results include an analysis on the potential savings compared to required input power, and, hence, no conclusive evidence of a net drag reduction has been reported.

Henoch and Stace[4] performed an experimental study of a Lorentz force generated by a spanwise array of electrodes and magnets, and showed the effects of the force on a turbulent boundary layer in seawater. This force is aligned with

[a]Author to whom correspondence should be addressed. Telephone: 310-825-4393; fax: 310-206-4830; electronic mail: jkim@seas.ucla.edu
[b]Present address: Department of Mechanical Engineering, University of Seoul, Korea; electronic mail: chlee@seoul.uos.ac.kr

 

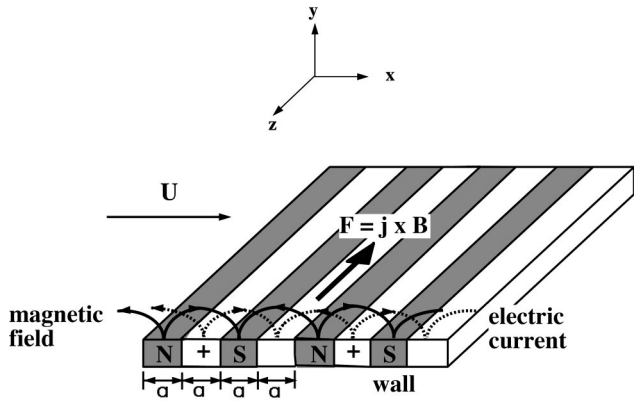


FIG. 1. Schematic of an arrangement for the creation of a Lorentz force along the spanwise direction. Note that temporal oscillation of the spanwise force can be generated by alternating the polarity of the electrodes in time.

the streamwise axis, and can act in either the upstream or downstream directions. Skin friction was found to increase, but this increase is offset by a gain in thrust. In addition, the boundary layer thickness decreases and the turbulence intensities are suppressed across the boundary layer. An interaction parameter was used to characterize different effects on the flow for low, moderate, and high magnitudes of the forcing. At low values of this quantity, it was found that only the near-wall region is influenced by the force. When the interaction parameter is larger, the mean flow is unaffected but the wall-shear stress fluctuations and turbulence intensity are suppressed in the lower part of the boundary layer by up to 30% of their unperturbed values. At the highest magnitude of forcing, skin friction and turbulence intensity are increased. As the mean velocity approached zero, the force only acted as a momentum pump. In all these cases, the force was directed in the downstream direction. For the upstream case, the mean velocity is reduced and the turbulence intensity increased.

Bandyopadhyay and Castano[9] performed an investigation using microtiles of miniature electrodes and magnets to control near-wall turbulence. Both experimental and numerical simulations were performed. The length and time scales of the microtiles were designed to match those of the near-wall small-scale turbulence structures at high Reynolds numbers. By pulsing the Lorentz force produced by an array consisting of five microtiles placed in the spanwise and streamwise directions, narrow hairpin vortices are superimposed on the mean flow. A simplified model was proposed to explain the effects of this force. It was postulated that pulsing the force creates a resonance condition similar to that produced by an oscillating-wall Stokes' layer. However, they found no reduction in skin-friction drag and did not specify the mechanism responsible for the drag reduction induced by the pulsating Lorentz force.

O'Sullivan and Biringen[10] attempted to identify the resonance mechanism in low Reynolds number numerical simulations, as proposed by Bandyopadhyay and Castano.[9] Four different tile cases were simulated. One of the cases was set up to reproduce the experimental microtiles of Bandyopadhyay and Castano.[9] It was found that the resulting Lorentz force was too weak to have an effect on a turbulent flow field. The second case was used to investigate the application of both static and pulsed-in-time force fields at two frequencies, in an attempt to find a resonance relationship between the force frequency and either the average burst frequency or the Stokes' layer frequency. Only a weak alteration of the mean drag (averaged over the wall) was observed. However, it was found that approximately 5% and 10% drag reduction occurred in the vicinity of the microtile actuators for the static and pulsed force fields, respectively. The third and fourth cases involved rotating the tiles 90° (about the wall–normal axis) from their orientation in the first two cases, thereby setting up a locally spanwise oscillating force field. They reported that for these two runs the drag decreased very slightly (on the order of 1%).[11] They also predicted that the Lorentz force produced by a microtile actuator would be more effective at higher Reynolds number, claiming the force magnitude scales as $1/u_\tau^2$, where $u_\tau$ is the wall-shear velocity, $u_\tau = \sqrt{\tau_{\text{wall}}/\rho}$.

Crawford and Karniadakis[5] performed a direct numerical simulation of the Henoch and Staces[4] spanwise array in a channel flow and also found only an increase in drag for this configuration. They were also able to analyze the Reynolds stress budgets and identify the terms responsible for the drag increase. The force distribution used in their calculation, however, appears to be nonphysical in that its sign changes with increasing distance from the wall. Their analysis is discussed in more detail in Sec. V.

In a different approach, Akhavan *et al.*[12] showed through numerical simulation that spanwise oscillatory motion of a wall or an oscillatory spanwise pressure gradient (they are equivalent in the channel) can suppress turbulence and the streamwise skin friction. Experiments with a spanwise oscillating surface were performed by Laadhari *et al.*,[13] and confirmed the numerical results of Akhavan *et al.*[12] Also, it is well known that when a two-dimensional boundary layer becomes three dimensional through a suddenly imposed pressure gradient or mean strain, it can experience an unexpected reduction in the turbulent kinetic energy and skin friction in the initial stages, despite the additional strain.[14–16] These results of Akhavan *et al.*[12], Sendstad and Moin[16] and Coleman *et al.*[15] contain a significant implication regarding boundary-layer control for drag reduction: that is, any sudden change in the mean strain disturbs the semiequilibrium state between the turbulence and the mean flow, leading to a reduction in the ability of turbulence to extract energy from the mean. The reduction in turbulence production, especially in the wall region, ultimately leads to a reduction in skin-friction drag.

Choi *et al.*[17] demonstrated through numerical experiments that when the near-wall streamwise vortices are suppressed through a closed-loop feedback control, a significant drag reduction (about 25%) can be achieved. A similar modification of the interaction between the streamwise vortices and the walls by longitudinal riblet surfaces has also been found to lead to a reduction in drag.[18] However, this reduction is much smaller than that obtained from the closed-loop control method. These results suggest that the key to drag

TABLE I. Parameters used to calculate power consumed by an array of electrodes and magnets. These values were chosen to match the parameters used by Nosenchuck *et al.*[7,8] However, because of the difference in the Reynolds number certain parameters were chosen arbitrarily to match others.

| $\mathrm{Re}_\tau$ | $\mathrm{Re}_x^{a}=\frac{U_\infty x}{\nu}$ | $\delta$ | $u_\tau$ | $U_\infty$ | $J_0$ | $V_0$ | $B_0$ | $P^*_{\mathrm{used}}$ | $P^*_{\mathrm{saved}}$ |
|---|---|---|---|---|---|---|---|---|---|
| 100 | $6\times10^4$ | 0.04 m | $0.0025\frac{\mathrm{m}}{\mathrm{s}}$ | $0.06\frac{\mathrm{m}}{\mathrm{s}}$ | $12.4\frac{\mathrm{A}}{\mathrm{m}^2}$ | 0.05 V | 0.6 T | $\sim10^4$ | $\sim8-10$ |

[a]$\mathrm{Re}_x\approx84\,\mathrm{Re}_\tau^{10/7}$.

reduction in both cases is alterating the interaction between the streamwise vortices and the wall.

In this paper we present results obtained from applying the Lorentz force to low Reynolds number turbulent channel flow. Different types of force configurations resulting from changes in the profile, direction, magnitude, oscillation period (temporal oscillation) and wave number (spatial oscillation) of the force distribution are considered. Direct numerical simulations of turbulent channel flow with different control schemes are conducted to explore various means of open- and closed-loop controls. Both realistic and idealized Lorentz force distributions are tested using open-loop control while only an idealized distribution is used with closed-loop control. The effect of an externally imposed (both steady and unsteady) Lorentz force on turbulence structures — streamwise vortices, in particular — has been investigated in order to explore new control strategies.

In Sec. II we discuss the governing equations for an electrically conducting, incompressible Newtonian fluid. In Sec. III we describe the numerical procedure employed to study the effect of the Lorentz force on a turbulent flow field. In Secs. IV, V, and VI we describe the open-loop control methods, while in Sec. VII we discusse the closed-loop control scheme in which an idealized Lorentz force is used to interactively reduce the drag. Concluding remarks are presented in Sec. VIII.

## II. GOVERNING EQUATIONS

The governing equations for an electrically conducting, magnetically permeable, incompressible Newtonian fluid are

$$\frac{\partial \mathbf{u}}{\partial t}+\mathbf{u}\cdot\nabla\mathbf{u}=-\frac{1}{\rho}\nabla p+\nu\nabla^2\mathbf{u}+\frac{1}{\rho}(\mathbf{J}\times\mathbf{B}), \tag{1}$$

$$\nabla\cdot\mathbf{u}=0, \tag{2}$$

$$\nabla\times\mathbf{E}=-\frac{\partial \mathbf{B}}{\partial t}, \tag{3}$$

$$\nabla\times\mathbf{B}=\mu_0\mathbf{J}_S, \tag{4}$$

$$\mathbf{J}=\sigma(\mathbf{E}+\mathbf{u}\times\mathbf{B}), \tag{5}$$

$$\nabla\cdot\mathbf{B}=0, \tag{6}$$

$$\nabla\cdot\mathbf{J}=0. \tag{7}$$

Here, $\mathbf{u}$ is the velocity vector, $p$ is the pressure, $\rho$ is the fluid density, $\nu$ is the kinematic viscosity, $\mathbf{B}$ is the magnetic flux density vector, $\mathbf{J}$ is the current density vector, $\mathbf{J}_S$ is the electrode source current density vector and is equal to the first term of the right-hand side of Eq. (5) [see Eq. (9)], $\mathbf{E}$ is the electric field vector, and $\mu_0$ and $\sigma$ are the magnetic permeability and the electrical conductivity of the fluid, respectively. The magnitude of $\mu_0$ is $\mathcal{O}(10^{-7})$, and, for low conductivity fluids like seawater, typical values of $\sigma$ are 2.5-5 Siemens, i.e., Ampère/V m. The first two equations are the Navier–Stokes equations and the latter five are the Maxwell equations, with the assumption that the electric field density and displacement current are negligible.

The equations governing the electric field are derived from Eq. (3) by neglecting the time-variation of the magnetic field, since no eddy currents are induced and only permanent magnets are being considered. For our specific application, the current density becomes directly proportional to the electric field vector $\mathbf{E}$, since the load factor, $\|\mathbf{E}\|/\|\mathbf{u}\times\mathbf{B}\|$, is much greater than 1. For example, Table I shows that $\|E\|\sim V_0/\delta$ has order 1 and $\|\mathbf{u}\times\mathbf{B}\|$ has order $10^{-3}$, giving a load factor value of approximately $10^3$. Here $V_0$ is the magnitude of the imposed voltage drop at the wall. Thus,

$$\nabla\times\mathbf{E}=0, \tag{8}$$

$$\mathbf{J}\simeq\mathbf{J}_S=\sigma\mathbf{E}. \tag{9}$$

Equations (8) and (9) imply that the electric field can be represented by a potential function, $\phi$, such that $\mathbf{J}=-\sigma\nabla\phi$. Combined with Eq. (7), the governing equation for $\phi$ becomes Laplace's equation,

$$\nabla^2\phi=0. \tag{10}$$

Equation (10) shows that the electrode current density vector, $\mathbf{J}$, can be represented as a gradient of a potential. Since the curl of the gradient of a function is zero, the right-hand side of Eq. (4) becomes zero after taking the curl,

$$\nabla\times(\nabla\times\mathbf{B})=-\mu_0\sigma(\nabla\times\nabla\phi), \tag{11}$$

$$\nabla(\nabla\cdot\mathbf{B})-\nabla^2\mathbf{B}=0. \tag{12}$$

The first term of Eq. (12) is zero from Eq. (6) and the governing equation for the magnetic flux density becomes

$$\nabla^2\mathbf{B}=0. \tag{13}$$

As shown above, the current induced by the flow is small. Also, it is assumed that the induced magnetic field is small compared to the applied magnetic field. As a result, the electric and magnetic fields are obtained by solving Eq. (10) and the dimensional form of Eq. (13) with appropriate

boundary conditions. The resulting force distribution can then be directly added as a body force term to the right-hand side of the Navier–Stokes equations.

The governing equations are placed in nondimensional form using the shear velocity, $u_\tau=\sqrt{(\tau_{\text{wall}}/\rho)}$, boundary layer thickness, $\delta$, and the current density and magnetic field values at the electrode and magnet surfaces, $J_0$ and $B_0$, respectively. Thus, the governing equations take the following nondimensional form:

$$\frac{\partial \mathbf{u}}{\partial t}+\mathbf{u}\cdot\nabla\mathbf{u}=-\nabla p+\frac{1}{\mathrm{Re}_\tau}\nabla^2\mathbf{u}+\mathrm{St}(\mathbf{J}\times\mathbf{B}), \tag{14}$$

$$\nabla\cdot\mathbf{u}=0, \tag{15}$$

where $\mathrm{Re}_\tau$ is the Reynolds number based on $u_\tau$ and $\delta$, and $\mathrm{St}=J_0B_0\delta/[\rho u_\tau^2]$ is the ratio of the Lorentz force to the inertia force of the fluid (a ratio commonly referred to as the Stuart number).

## III. DIRECT NUMERICAL SIMULATIONS

Direct numerical simulations are carried out for low Reynolds number turbulent channel flow fields to determine the effectiveness of the Lorentz-force flow control. All simulations are performed using constant mass flux. Periodic boundary conditions are used in the streamwise and spanwise directions while the usual no-slip boundary conditions are enforced at the walls. Both a Chebyshev-tau method in the wall–normal direction and a dealiased Fourier method were used in the streamwise and spanwise directions to solve the Navier–Stokes equations. A semi-implicit time advancement scheme is employed by using the second-order Crank–Nicolson implicit method for the viscous terms and an explicit Runge–Kutta third-order scheme for the nonlinear and body force terms. More details may be found in Kim *et al.*[19] Note that all wall units used throughout this paper are referenced with respect to initial conditions before any control is applied. The $\mathrm{Re}_\tau=100,200,400$ range is tested in the following sections. For these three Reynolds numbers, the domains extend $4\pi\delta\times2\delta\times4\pi\delta/3$, $2\pi\delta\times2\delta\times4\pi\delta/3$, and $\pi\delta\times2\delta\times\pi\delta/3$ in the streamwise, wall–normal, and spanwise directions with grid sizes of $32\times65\times32$, $64\times65\times64$, and $64\times129\times64$, respectively. The resolution and box size for the $\mathrm{Re}_\tau=400$ case, $\pi\delta\times2\delta\times\pi\delta/3$, and $64\times129\times64$, respectively, are marginal at best. However, a few test cases using higher resolution and larger box size have been carried out and the results indicate the same drag reduction trend. We therefore conclude that, for our purposes, a box size of $\pi\delta\times2\delta\times\pi\delta/3$ using a grid size of $64\times129\times64$ is adequate. Before applying any control, all simulations are allowed to develop until the turbulent flow fields reach statistical equilibrium. Results are compared with other researchers' findings when possible.

## IV. OPEN-LOOP CONTROL: ''IDEALIZED'' LORENTZ FORCE

### A. Spanwise oscillating Lorentz force

We start with the premise that the key to drag reduction is to disturb the semiequilibrium state between the near-wall streamwise vortices and the wall. We further postulate that an effective way to achieve this goal is to introduce Lorentz force perturbations perpendicular to the vortices. An open-loop control scheme is implemented: spanwise Lorentz forcing is introduced into the flow with no feedback from the flow to the forcing. The Lorentz force DNS channel results are compared with those from a regular channel flow[19] in order to investigate the effect of the electromagnetic forcing on wall-bounded turbulence. Further comparisons with other forms of turbulence control (e.g., Choi *et al.*[17], Akhavan *et al.*[12]) are shown in later sections.

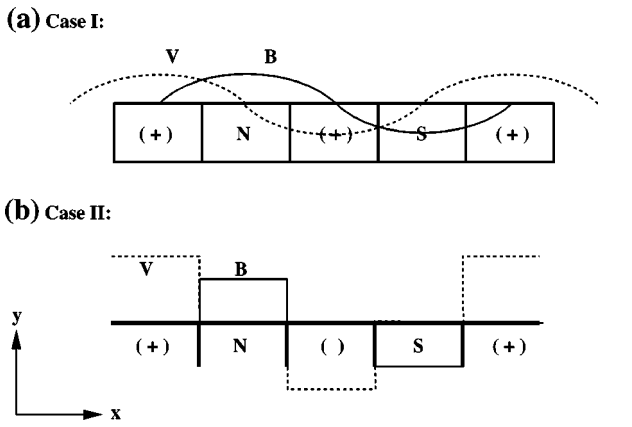


FIG. 2. Two array configurations used to study the efficiency of a realistic force distribution: (a) Sinusoidal electric/magnetic field distributions (i.e., idealized case); (b) one period using Dirichlet boundary conditions for each electrode and magnet, and Neumann boundary conditions between each electrode and magnet, with equal electrode and magnet spacing.

The required Lorentz force can be created by placing electrodes and magnets side by side, parallel to one another, as shown in Fig. 1. This configuration is similar to that used by Gailitis and Lielausis[2] and Tsinober and Shtern.[3] In their investigations, however, this array was oriented parallel to the flow direction, producing primarily a streamwise force. In contrast, the primary Lorentz force component in the current configuration acts in the spanwise direction, such that it is always perpendicular to the axes of the near-wall streamwise vortices.

Two cases in which an array of alternating electrodes and magnets produces a spanwise Lorentz force were studied, each with the same power consumption; Fig. 2 illustrates the electrode and magnet configuration for both. Case I assumes a sinusoidal variation of both the electric and magnetic potential distributions on the surface, and the resulting force field is constant in the spanwise direction and decays exponentially in the wall–normal direction (see the Appendix). The rate of decay is determined by the width of the electrodes and magnets. Time oscillation can be accomplished by alternating the polarity of the electrodes in time. We shall refer to case I as an ''idealized'' force to distinguish it from case II, the ''realistic'' one. Case II represents the realistic force with Neumann boundary conditions for the electric field placed on the magnet surfaces between the electrodes and on the electrode surfaces for the magnetic field; Dirichlet boundary conditions were imposed on each electrode and magnet surface. More details of this formulation are discussed in Sec. V.

At the wall, the nondimensional spanwise force is written in terms of the applied voltage, $V_0$ (which is a more convenient quantity than the current density, $J_0$), such that

$$f_z^+ = \frac{\pi}{4}\frac{\delta}{a}\frac{\sigma V_0 B_0}{\rho u_\tau^2} f_z, \tag{16}$$

where $a$ is the electrode and magnet width, $V_0 = 4a/[\pi\sigma J_0]$ is the total voltage drop at the wall, and $B_0$ is the magnetic flux density at the wall. The ''+'' superscript indicates variables that have been nondimensionalized by wall-unit scales from the initial (undisturbed) flow. The spanwise force oscillates in time and decays exponentially in the wall–normal direction,

$$f_z^+ = \mathrm{St}\exp\left(-\frac{\pi y^+}{a^+}\right)\sin\left(\frac{2\pi t^+}{T^+}\right). \tag{17}$$

The parameter $T^+$ is the period of oscillation, and $a^+$ (the magnet and electrode widths, which here are assumed to be the same) sets the distance the force penetrates into the flow. Recall that St is the relative strength of the Lorentz force with respect to the inertia force (see Sec. II). Equation (17) is expected to have the same effect as the spanwise wall oscillation imposed by Akhavan *et al.*[12] However, the present control is placed within the near-wall region only, whereas the Akhavan *et al.*[12] spanwise oscillation pressure gradient extends the full height of the channel. From an energy standpoint, it is often impractical to effect control over the entire flow domain.

### B. Results and discussion

The initial runs were carried out at a low Reynolds number, $\mathrm{Re}_\tau = 100$. Several combinations of oscillation period, $T^+$, penetration depth, $a^+/\pi = \Delta^+$, and Stuart number, St, were considered. The penetration depth, $\Delta^+$, was set to 10 for the first run. This value causes the force to decay to 5% of the maximum force value at a distance of 30 wall units away from the wall in the initial flow. The maximum force value is located at the wall. This choice of penetration depth, $\Delta^+ = 10$, was based on the model by Kim *et al.*[19] (their Fig. 15) in order to have the greatest effect on the near-wall turbulence structures responsible for high-skin friction—namely, streamwise vortices, the centers of which are located at approximately $y^+ = 15$–$25$ away from the wall. The Stuart number was set to $20\pi$ so that the Lorentz force will be of the same order of magnitude as the effective spanwise pressure gradient applied by Akhavan *et al.*[12] The oscillating wall/pressure-gradient study also provides guidance for defining the Lorentz-force oscillation period $T^+$. Since Akhavan *et al.*[12] found a maximum streamwise drag reduction when their spanwise wall (or pressure gradient) oscillated with a period of 100 wall units and the drag increased for larger or smaller values, we use $T^+ = 100$ and 500 for the present computations.

Figure 3 shows the drag history after a spanwise oscillating Lorentz force has been applied to a turbulent channel flow with $\mathrm{Re}_\tau = 100$, $\Delta^+ = 10$, and $T^+ = 100$ and 500. The no-control case is presented for comparison purposes. It can be clearly seen how, at this Reynolds number, a spanwise oscillatory Lorentz force can significantly reduce the drag for $T^+ = 100$, but not for $T^+ = 500$, a result consistent with that of Akhavan *et al.*[12] Note, however, that here the current Lorentz force is confined to the near-wall region, in contrast to the Akhavan *et al.*[12] control, for which the applied spanwise pressure gradient (equivalent to wall oscillation) spans over the entire channel height. This result suggests that modification of near-wall turbulence structures alone is sufficient to achieve drag reduction. The drag is reduced by approximately 40% under these conditions.

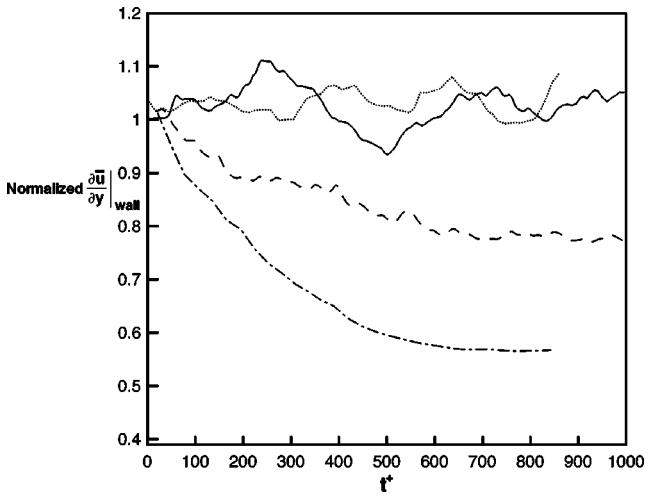


FIG. 3. Drag histories for $\mathrm{Re}_\tau = 100$ channel with $\Delta^+ = 10$: no control, —; $T^+ = 100$ and $\mathrm{St} = 10\pi$, ---; $T^+ = 100$ and $\mathrm{St} = 20\pi$ –·–; $T^+ = 500$ and $\mathrm{St} = 20\pi$, ···.

Figure 4 shows plots of instantaneous streamwise vorticity for the no-control, $T^+ = 100$ and $T^+ = 500$ cases (control is applied only to the upper wall). These plots reveal that most of the near-wall streamwise vortices are suppressed when $T^+ = 100$, but not when $T^+ = 500$. These results confirm our premise that the key to drag reduction is to perturb the near-wall streamwise vortices in turbulent boundary layers. For the $T^+ = 100$ case, the streamwise vortices near the control wall are significantly suppressed, resulting in a substantial drag reduction; on the other hand, when $T^+ = 500$, the streamwise vortices are not affected by the oscillating Lorentz force, resulting in no drag reduction. The hypothesis for drag being reduced for $T^+ = 100$ but not for $T^+ = 500$ will be discussed further below.

To more clearly illustrate the spanwise-Lorentz force effects, a comparison is made of turbulence statistics from the controlled and uncontrolled flows. Figure 5 shows both the mean velocity profile for $T^+ = 100$ and the effect of the idealized force, Eq. (17), upon the mean wall shear. The mean velocity is nondimensionalized with respect to the initial reference velocity. A typical trend of drag-reduced turbulent flows is demonstrated by this figure in which the slope of the mean profile near the control wall is reduced. Figure 6 illustrates the mean velocity profile on the control side nondimensionalized with respect to the shear velocity of the no-control case versus the wall normal distance in wall units. By the increase in the mean velocity profile, $u^+$, it clearly reveals that $u_\tau$ decreases for the control case with $T^+ = 100$,

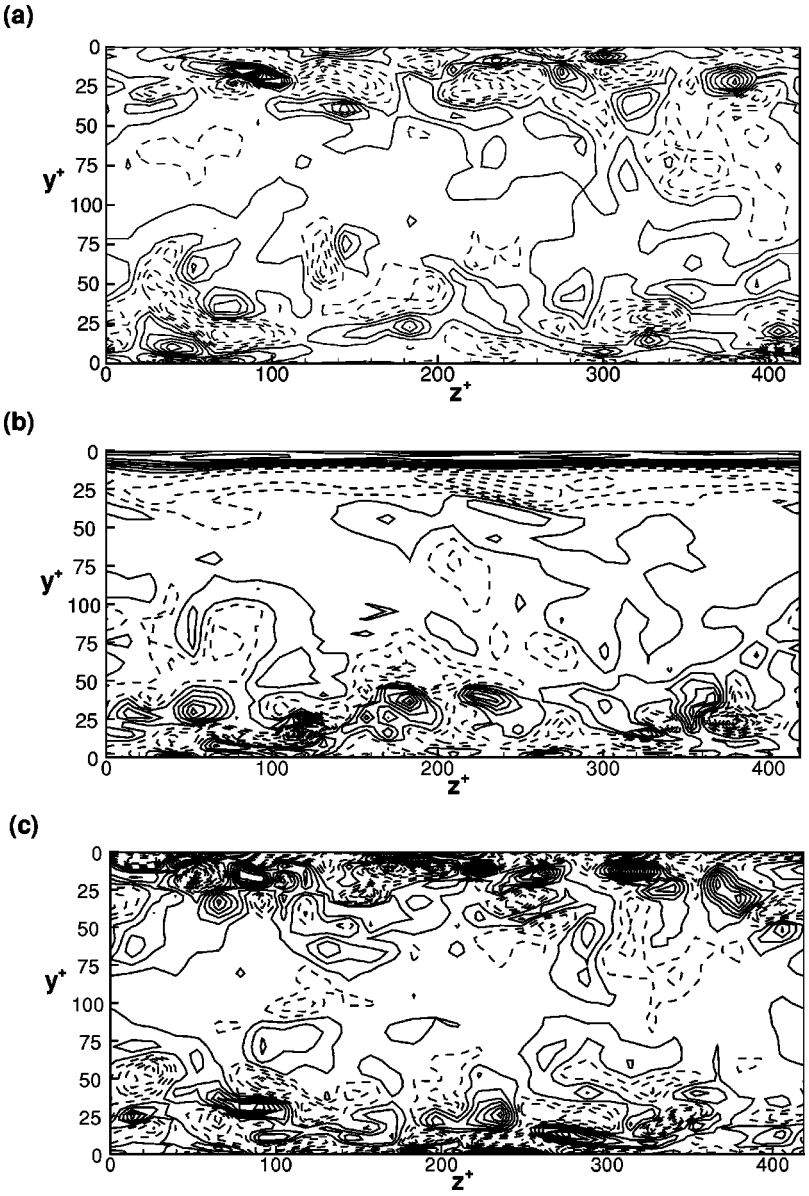


FIG. 4. Contours of streamwise vorticity, $\omega_x$, shown for $\mathrm{Re}_\tau=100$: (a) no control; (b) $T^+=100$, $\Delta^+=10$, $\mathrm{St}=20\pi$; (c) $T^+=500$, $\Delta^+=10$, $\mathrm{St}=20\pi$. Note that for $T^+=100$ the streamwise vortices are nearly completely suppressed. Dashed lines indicate negative values. (Lorentz force applied at top wall only.)

$\mathrm{St}=20\pi$, and $\Delta^+=10$. The rms velocity fluctuations on the control side of the channel are presented in Fig. 7. Each component is nondimensionalized with respect to the initial reference velocity. A significant decrease in all three velocity components is observed, which implies that a Lorentz force localized to act upon the near-wall structures can profoundly reduce the kinetic energy of the turbulence.

Although the present results indicate that the Lorentz force can be used to achieve substantial drag reduction, the true measure of whether this control method is effective is obtained by considering the amount of power required to produce the spanwise Lorentz force and comparing it to the amount of power saved. Throughout the paper, the term ''efficiency,'' $\eta$, will indicate the ratio of the power saved due to drag reduction relative to the power used to create the required Lorentz force,

$$\eta=\frac{P_{\mathrm{saved}}}{P_{\mathrm{used}}}. \tag{18}$$

The power saved due to drag reduction is calculated by multiplying the ratio of the percent drag reduction by the friction force and mean velocity,

$$P_{\mathrm{saved}}=\frac{\Delta C_f}{C_f}\rho u_\tau^2 U_{\mathrm{cl}} A, \tag{19}$$

where $C_f=\tau_{\mathrm{wall}}/[\frac{1}{2}\rho U_{\mathrm{cl}}^2]$ is the skin-friction coefficient, $\tau_{\mathrm{wall}}$ is the wall shear stress, $U_{\mathrm{cl}}$ is the mean channel centerline velocity, $A$ is the area over which the Lorentz force control is affected, and $\Delta C_f$ is the amount of $C_f$ change due to the application of the Lorentz force. Scaling by the energy of the friction force on the wall, the nondimensionalized power saved, $P^*_{\mathrm{saved}}$, is

$$P^*_{\mathrm{saved}}=\frac{P_{\mathrm{saved}}}{\rho u_\tau^3 A}, \tag{20}$$

$$=\frac{\Delta C_f}{C_f}\frac{U_{\mathrm{cl}}}{u_\tau}. \tag{21}$$

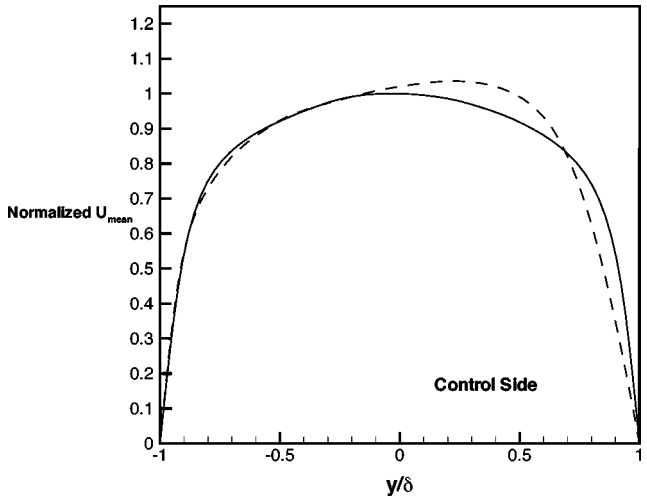


FIG. 5. Mean velocity profile for a spanwise oscillating Lorentz force for $\mathrm{Re}_\tau=100$: no control, —; $\mathrm{St}=20\pi$, $\Delta^+=10$ and $T^+=100$, ---.

(A ''*'' superscript will be used throughout to denote a nondimensional quantity.)

Next, the amount of power required to produce the spanwise Lorentz force is calculated by

$$P_{\text{used}}=VI_{\text{rms}}, \tag{22}$$

where $V$ is the voltage distribution and $I_{\text{rms}}$ is the rms value of the current distribution over the control wall:

$$P^*_{\text{used}}=\frac{P_{\text{used}}}{\rho u_\tau^3 A}, \tag{23}$$

$$=\frac{V_0 J_0 A_e}{\rho u_\tau^3 A}. \tag{24}$$

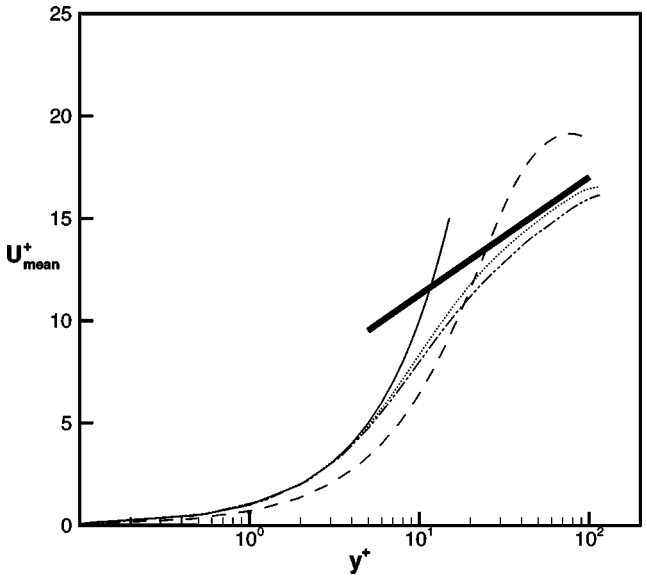


FIG. 6. Mean velocity profile on the control side of the channel in terms of wall units for a spanwise oscillating Lorentz force for $\mathrm{Re}_\tau=100$, $\Delta^+=10$: no control, ···; $u^+=y^+$, —; $u^+=2.5\ln(y^+)+5.5$, —; $\mathrm{St}=20\pi$ and $T^+=100$, ---; $\mathrm{St}=4\pi$ and $T^+=500$, –···–.

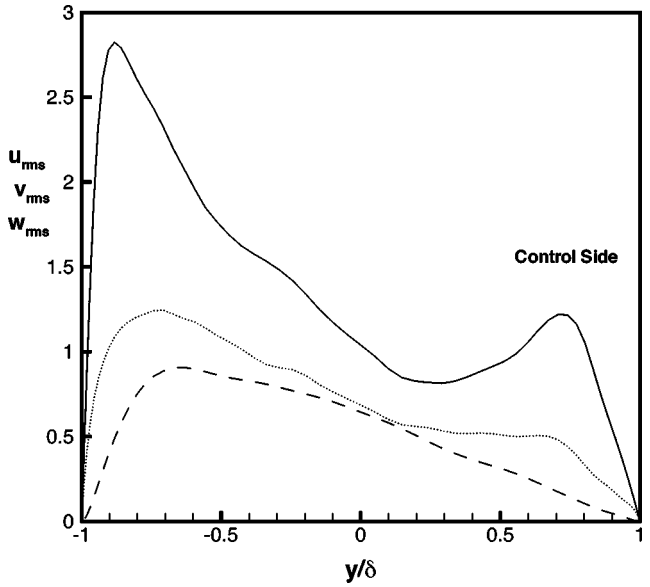


FIG. 7. Root-mean-square velocity fluctuations for a spanwise oscillating Lorentz force for $\mathrm{Re}_\tau=100$, $\mathrm{St}=20\pi$, $\Delta^+=10$, and $T^+=100$: $u_{\text{rms}}/u_\tau$, —; $v_{\text{rms}}/u_\tau$, ---; $w_{\text{rms}}/u_\tau$, ····. The rms values are normalized by $u_\tau$ of the uncontrolled channel.

$A_e$ is the wetted surface area of an electrode, $V_0$ is the imposed voltage drop at the wall, and from the definition of the Stuart number $J_0=\mathrm{St}\,\rho u_\tau^2/[\delta B_0]$, assuming the current density field varies as a continuous sine function (see Sec. IV A). Table I lists the values used to estimate $P^*_{\text{used}}$, which is seen to be three orders of magnitude larger than $P^*_{\text{saved}}$, indicating that this form of control is not efficient, since $\eta$ is on the order of $10^{-3}$. Although this analysis is rather crude and the current electrode and magnet array configuration was not optimized to yield the best performance, the fact that $\eta$ is much smaller than 1 nevertheless suggests that it is unlikely that a net savings can be achieved with a similar spanwise Lorentz force approach. The primary cause of this ineffeciency is the low conductivity of seawater.

Further computations were carried out to investigate the effectiveness of this type of control on higher Reynolds number flows. The motivation for performing these experiments stems from an earlier study conducted by Nosenchuck,[8] which indicates that the required Stuart number (referred to as ''interaction parameter'' by Nosenchuck[8]) might decrease with an increasing Reynolds number. Utilizing the same $T^+=100$ and $\Delta^+=10$ values found to give the best results for $\mathrm{Re}_\tau=100$, DNS experiments were carried out at $\mathrm{Re}_\tau=200$ and 400. Results are summarized in Fig. 8, which shows that the St must be increased to attain a $C_f$ decrease—and the decrease that does occur is smaller—as $\mathrm{Re}_\tau$ increases for $T^+=100$ cases. As a result, the efficiency parameter, $\eta$, becomes smaller as $\mathrm{Re}_\tau$ increases. Runs with $T^+=500$ yielded similar results for $\mathrm{Re}_\tau=200$ and 400 as found at $\mathrm{Re}_\tau=100$, with the skin-friction increasing compared to the no-control case.

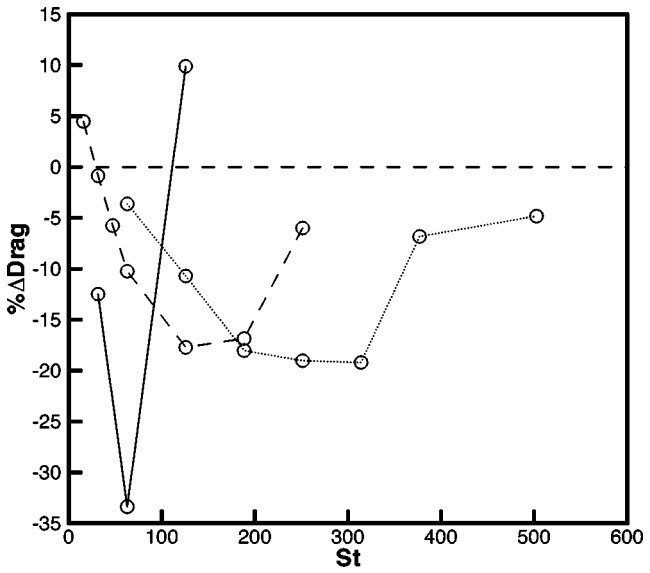


FIG. 8. Reynolds number dependence for $\Delta^+=10$ and $T^+=100$. The forcing required to achieve the same amount of drag reduction increases with $\mathrm{Re}_\tau$: $\mathrm{Re}_\tau=100$, —; $\mathrm{Re}_\tau=200$, ---; $\mathrm{Re}_\tau=400$, ⋯.

Thus, it appears that the required forcing increases with Reynolds number, but that an optimal oscillatory period appears to exist for a fixed magnet spacing. However, total efficiency does not improve with increasing Reynolds number in contrast to the trend reported by Nosenchuck[8] and the conjecture of O'Sullivan and Biringen.[10]

To investigate the dependence of these results on Reynolds number and oscillation period, a simplified analysis was performed by solving the mean spanwise momentum equation. Studies of three-dimensional boundary layers show that the contribution of $\overline{v'w'}$ takes a longer time to evolve than $\overline{u'v'}$.[20] Thus, the analysis is performed by considering a temporally oscillating, exponentially decaying (away from the wall) body force in a laminar flow, even though control is applied to a turbulent flow, and by ignoring the higher-order nonlinear terms. The governing equation for the mean spanwise velocity then becomes

$$\frac{\partial W^+}{\partial t^+}=\frac{\partial^2 W^+}{\partial y^{+2}}+\frac{\mathrm{St}}{\mathrm{Re}_\tau}\exp\left(-\frac{y^+}{\Delta^+}\right)\sin\left(\frac{2\pi t^+}{T^+}\right), \tag{25}$$

subject to

$$W^+(y^+=0,t^+)=0, \tag{26}$$

$$W^+(y^+\to\infty,t^+)=0. \tag{27}$$

This is similar to Stokes' oscillating plate problem. However, here the wall is fixed in time with the fluid being oscillated by the Lorentz force, and the force penetration depth is a free parameter that can be prescribed *a priori*. Let

$$\hat{y}^+\equiv y^+\sqrt{\frac{\pi}{T^+}}, \tag{28}$$

$$\tilde{y}^+\equiv\frac{y^+}{\Delta^+}, \tag{29}$$

$$\tilde{\Delta}^2\equiv\frac{\Delta^{+2}}{\sqrt{1+\dfrac{4\Delta^{+4}\pi^2}{T^{+2}}}}. \tag{30}$$

The nondimensional envelope of the real part of the solution for $W^+(y^+,t^+)$ is

$$W^+_{\mathrm{env}}=\frac{\mathrm{St}\,\tilde{\Delta}^2}{\mathrm{Re}_\tau}\{\exp(-2\hat{y}^+)+\exp(-2\tilde{y}^+)-2\cos(\hat{y}^+)\exp[-(\tilde{y}^++\hat{y}^+)]\}^{1/2}. \tag{31}$$

Thus, the maximum spanwise velocity near the wall is proportional to the magnitude of the forcing, as expected, but is inversely proportional to the Reynolds number,

$$W^+_{\mathrm{env}}\big|_{\max}\propto\frac{\mathrm{St}\tilde{\Delta}^2}{\mathrm{Re}_\tau}. \tag{32}$$

Therefore, in order to affect the near-wall structures with fixed $\Delta^+$ and $T^+$, the forcing must increase proportionally with Reynolds number. This result has been verified by our DNS turbulent channel flow experiments. Plots of the mean induced spanwise velocity from the optimal case of $\mathrm{Re}_\tau=100$, $T^+=100$, $\Delta^+=10$, and $\mathrm{St}=20\pi$, and the analytic solution for $W^+_{\mathrm{env}}$ [Eq. (31)] are shown in Fig. 9. The two plots are very similar to each other, supporting the assertion that the induced spanwise velocity scales inversely with the Reynolds number. It can be seen that the ideal force in Eq. (25) creates a strong spanwise jet in the near-wall region, a result found for each case listed in Table II.

Having demonstrated that a drag reduction can be obtained, we now seek to more accurately quantify the effect of the parameters on the reduction. Additional computations were therefore made for various combinations of oscillation period, $T^+$, penetration depth, $\Delta^+$, Reynolds number, $\mathrm{Re}_\tau$, and force magnitude, St. The ranges of the four independent parameters are given in Table II. Three values of $\Delta^+$, 5, 10, and 20, were tested in order to have the greatest effect on the near-wall turbulence structures. For a higher Reynolds number, it can be seen that drag reduction is fairly insensitive to $\Delta^+$, except for a very low Reynolds number case ($\mathrm{Re}_\tau=100$) in which the interaction between the two walls is more pronounced. It was found that an optimal oscillation period exists for various magnitudes of the other three parameters ($\mathrm{Re}_\tau$, $\Delta^+$, and St). Specifically, a range of $T^+=50-100$ produced the greatest amount of drag reduction for all values of $\mathrm{Re}_\tau$, $\Delta^+$, and St considered (Figs. 10 and 11). This range is consistent with results from Coleman *et al.*[15] in the case of two-dimensional (2-D) turbulent channel flows at $\mathrm{Re}_\tau=180$ imposed to a suddenly moving wall. They found that the largest amount of drag reduction occurs approximately $t^+=50-100$ time units after the strain is introduced [their Fig. 2(a)]. In the present computations, it was found that periods of $T^+=25$ and 125 were not as effective in reducing the drag as were $T^+=50-100$, leading to the conclusion that open-loop near-wall control using a spanwise oscillation force reduces the drag for a certain range of span-

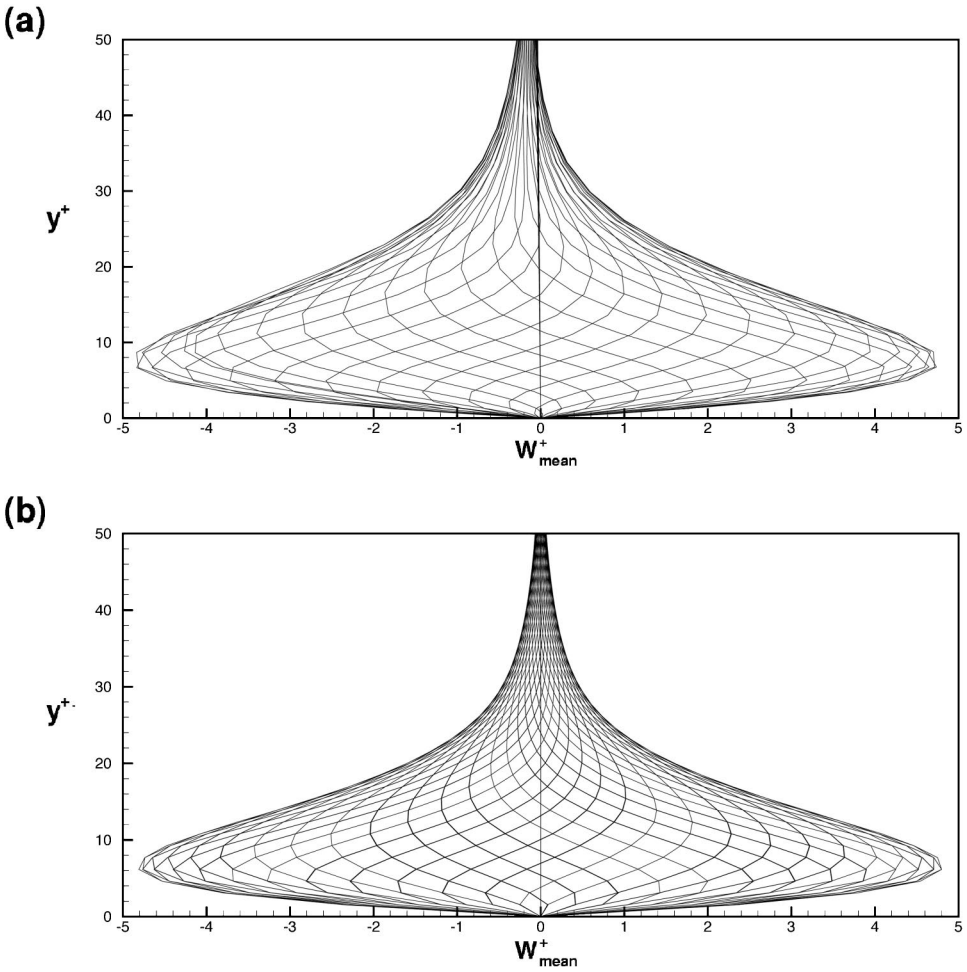


FIG. 9. Induced spanwise velocity profiles: (a) turbulent case; (b) analytical solution of Eq. (25). The different curves represent different instances in time during the forcing period.

wise oscillation frequencies. However, the values of St needed to obtain this reduction are too large for us to conclude that this open-loop control scheme will lead to a net power savings.

The oscillating near-wall spanwise force has been shown to suppress the streamwise vortices, leading to a reduction in skin-friction drag (see Fig. 4). We hypothesize that the specific mechanism causing the drag reduction is application of mean shear to the near-wall vortices such that the vortices with the same sign as the applied shear survive, while the vortices of opposite sign are suppressed. During the next phase of the oscillating force, when the mean spanwise shear has changed sign, the remaining vortices are suppressed. If this model is correct, the oscillating force must satisfy two necessary conditions in order to suppress the vortices. First, the shear caused by the force must be large enough to overcome the natural dynamics of the vortices. Second, the shear must be applied in a location where the streamwise vortices are found. The second condition can be satisfied by selecting appropriate parameters for the spanwise body force. From Eq. (31), we see that the envelope of $W^+$ defines two kinds of boundary layers. One has a thickness of $\Delta^+$ and the other of $\sqrt{T^+}$. Since the near-wall structures scale with wall units, the optimum values of $\Delta^+$ and $\sqrt{T^+}$ are expected to be independent of Reynolds number.

From Eqs. (30) and (31), when $(2\Delta^{+2}\pi/T^+)^2 \gg 1$,

TABLE II. Parameters used in a parametric study using an open-loop spanwise oscillating Lorentz force.

| | $\mathrm{Re}_\tau=100$ | | $\mathrm{Re}_\tau=200$ | | $\mathrm{Re}_\tau=400$ | |
|---|---|---|---|---|---|---|
| $\Delta^+$ | $T^+$ | St | $T^+$ | St | $T^+$ | St |
| 5 | 50 | $20\pi$ | 50 | $20\pi$ | 50 | $40\pi$ |
| | 100 | $20\pi$ | | $40\pi$ | | $80\pi$ |
| | | | | $80\pi$ | | $120\pi$ |
| | | | 100 | $20\pi$ | 100 | $40\pi$ |
| | | | | $40\pi$ | | $80\pi$ |
| | | | | $80\pi$ | | $120\pi$ |
| 10 | 25 | $20\pi$ | 50 | $20\pi$ | 50 | $40\pi$ |
| | | $80\pi$ | | $40\pi$ | | $80\pi$ |
| | 50 | $20\pi$ | | $80\pi$ | | $120\pi$ |
| | | $40\pi$ | 100 | $20\pi$ | 100 | $40\pi$ |
| | 75 | $20\pi$ | | $40\pi$ | | $80\pi$ |
| | 100 | $20\pi$ | | $80\pi$ | | $120\pi$ |
| | 125 | $20\pi$ | | | | |
| | 200 | $10\pi$ | | | | |
| | 500 | $4\pi$ | | | | |
| | | $20\pi$ | | | | |
| 20 | 50 | $20\pi$ | 50 | $20\pi$ | 50 | $40\pi$ |
| | 100 | $20\pi$ | | $40\pi$ | | $80\pi$ |
| | | | | $80\pi$ | | $120\pi$ |
| | | | 100 | $20\pi$ | 100 | $40\pi$ |
| | | | | $40\pi$ | | $80\pi$ |
| | | | | $80\pi$ | | $120\pi$ |

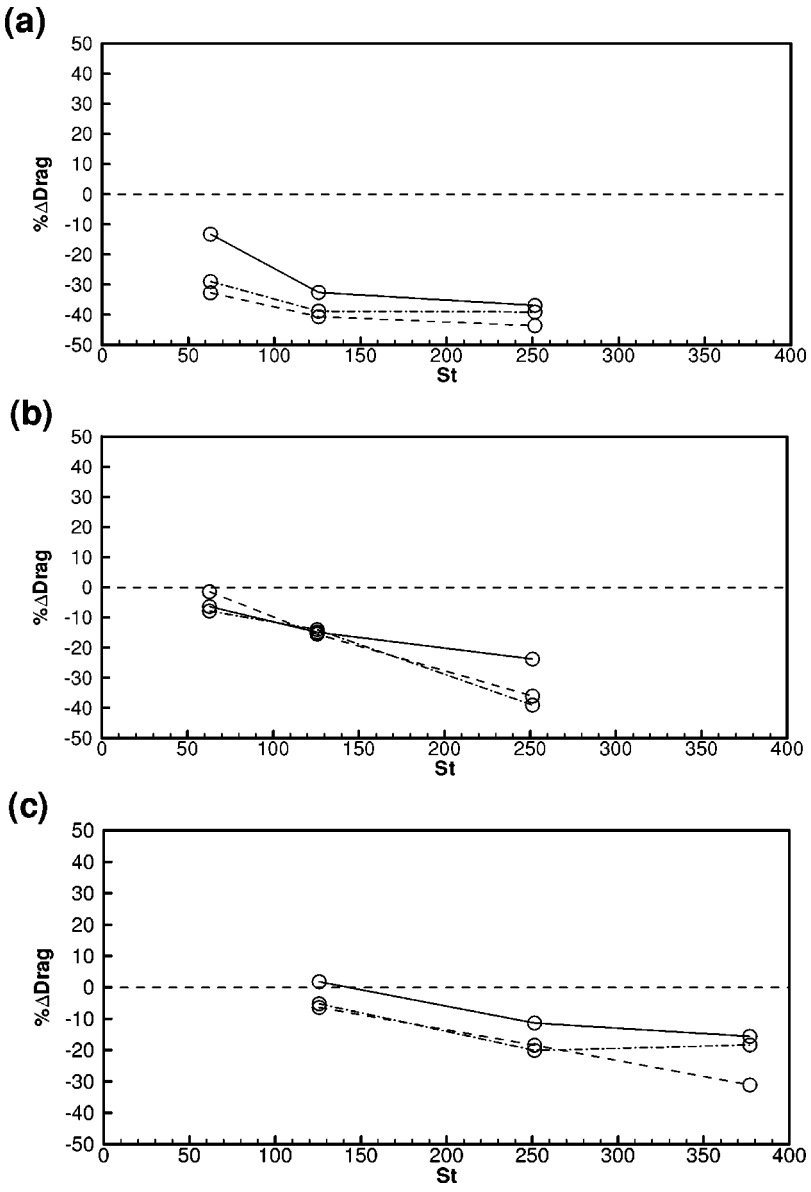


FIG. 10. Results of parametric study of drag reduction for oscillation frequency, $T^+=50$: (a) $\mathrm{Re}_\tau=100$; (b) $\mathrm{Re}_\tau=200$; (c) $\mathrm{Re}_\tau=400$. It can be seen that the St required to obtain the same amount of drag reduction increases with increasing $\mathrm{Re}_\tau$ and that an optimal value of St exists for a given $T^+$: $\Delta^+=5$, —; $\Delta^+=10$, ---; $\Delta^+=20$, $-\cdot-$.

$$W^+_{\mathrm{env}}|_{\max} \propto \frac{\mathrm{St}\, T^+}{\mathrm{Re}_\tau}. \tag{33}$$

This parameter must have an optimum value: too small a shear does not influence the near-wall structures and too big a shear may cause its own instability, as it does in the case of the Kelvin–Helmholtz instability.[21] Normalizing by $\pi$, Fig. 12 demonstrates that

$$\left(\frac{\mathrm{St}\, T^+}{\mathrm{Re}_\tau\, \pi}\right)_{\mathrm{opt}} \approx 20, \tag{34}$$

implying that the required St is proportional to the Reynolds number, since $T^+$ has a fixed optimal range. Also, Fig. 12 shows that $\mathrm{St}\, T^+/(\mathrm{Re}_\tau \pi)=40$ and 80 produce an equal amount of drag reduction to the 20 case but can also produce drag increase as well, which cannot be seen for the 20 case.

## V. OPEN-LOOP CONTROL: "REALISTIC" FORCE CASE

The Lorentz force we have used up to this point is idealized, in that it is obtained from artificial boundary conditions (the Appendix). Naturally, the next step in the analysis is to solve Maxwell equations directly in order to calculate a realistic force distribution and to compare the drag-reducing characteristics of this force to that of the approximate force distribution described in the previous section. Calculation of the realistic force was carried out by utilizing the exact boundary conditions for the electrode and magnet surfaces for an alternating array placed in the streamwise direction (Fig. 1). That is, for the electric/magnetic field, Dirichlet boundary conditions were imposed on each electrode/magnet, while Neumann boundary conditions were imposed in between, on each magnet/electrode.

In the Appendix we illustrate the solution of the Max-

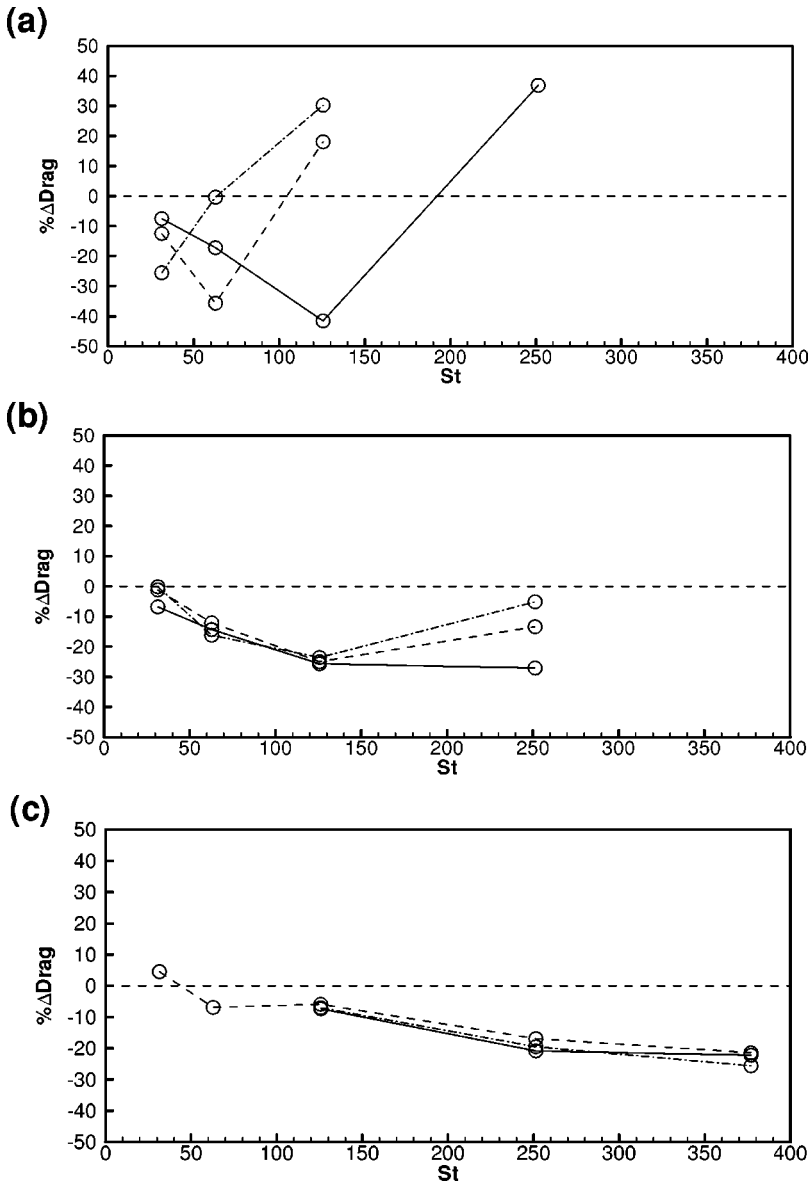


FIG. 11. Results of the parametric study of drag reduction for oscillation frequency, $T^+=100$: (a) $\mathrm{Re}_\tau=100$; (b) $\mathrm{Re}_\tau=200$; (c) $\mathrm{Re}_\tau=400$. It can be seen that the St required to obtain the same amount of drag reduction increases for increasing $\mathrm{Re}_\tau$ and that an optimal value of St exists for a given $T^+$: $\Delta^+=5$, —; $\Delta^+=10$, ---; $\Delta^+=20$, $-\cdot-$.

well equations using a sinusoidal variation of the fields on the electrode and magnet surfaces. However, this boundary condition is not physical since it creates a normal component on each nonconducting surface (only surface-parallel components should exist on nonconducting surfaces and only surface normal components should exist on electrodes). Two methods of imposing the boundary conditions were tested.

First, a numerical scheme was developed in order to impose Neumann boundary conditions for the potential functions on the nonconducting surfaces, and to impose Dirichlet boundary conditions on the conducting ones (for this analysis, we assume the electrode can conduct only electric current and likewise for the magnet with regard to magnetic flux). Crawford and Karniadakis[5] chose to use polynomial functions to define the electrode and magnet boundary conditions. Instead, a hybrid step-function/tan($x$) distribution was utilized in this study (Fig. 13). A step-function approach was used on conducting surfaces and a tan($x$) distribution was used between conductors to approximate the wall–normal gradient of the potentials to be zero. A $640\times129$ grid was used in the streamwise and wall–normal directions, respectively. The resulting components of current density **J** are also shown in Fig. 13, illustrating that the electrodes are representative of line sinks/sources. Similar results were derived for the magnetic flux density field, **B**. For an alternating array of electrodes and magnets with each electode activated continuously, the cross product of the force distribution must be unidirectional. The force distribution defined by this **J** and **B** is shown in Fig. 14. Note that there is no negative forcing, in contrast to that of Crawford and Karniadakis.[5] The force is all of one sign, indicating that this approach is more plausible for determining the effect of a realistic force created by an array geometry.

The second method of applying the boundary conditions was to perform a finite element analysis using ANSYS,[22] a general purpose finite element solver. A scalar potential analysis was done with the Neumann boundary conditions imposed automatically by ANSYS on the nonconducting surfaces. Two cases were created: one with a constant scalar potential value specified on the conducting surface of the

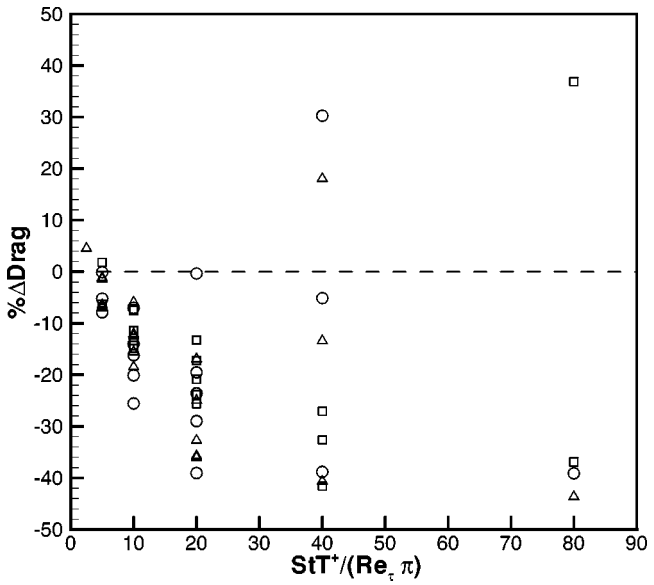


FIG. 12. Magnitude of Eq. (34), St $T^+/(\mathrm{Re}_\tau \pi)$, compared to the amount of percent drag reduction. For the cases considered, it can be seen that a value of 20 is most effective at reducing the drag: □, $\Delta^+=5$; △, $\Delta^+=10$; ○, $\Delta^+=20$.

magnet, and the other using nodes and elements to realistically model the subsurface magnets with appropriate material properties. A total of 8586 nodes and 16640 elements were used to represent the seawater region. A potential drop of 20 V was imposed on the surface of the electrodes and a conductivity of $\sigma=4.5$ Siemens was used (a typical value for seawater). The magnets were modeled using the material properties table option in ANSYS. The resulting electric and magnetic flux density fields from ANSYS were found to compare reasonably well with those calculated by the tan($x$) numerical method, despite the fact that the ANSYS solution used a much coarser grid. We conclude that the proper boundary conditions for the electric and magnetic potential functions

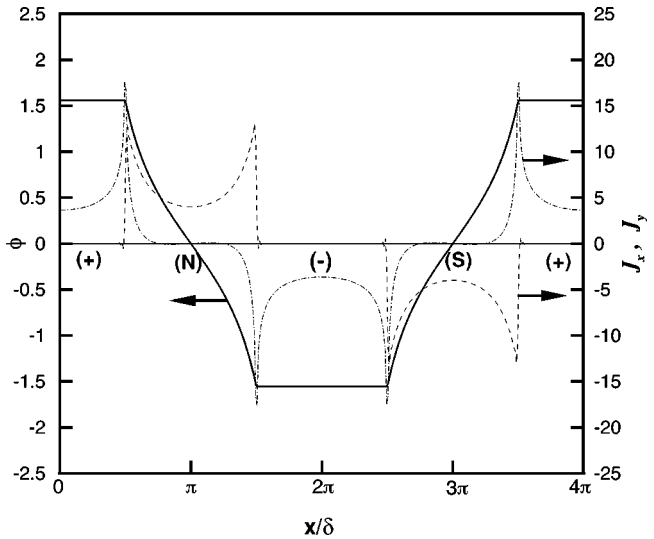


FIG. 13. Electric field potential $\phi$ and current density $\mathbf{J}=-\sigma\nabla\phi$ defined by step-function/tangent distribution. The variation of the magnetic field (not shown) is similar: $\phi$, —; $J_x$, ---; $J_y$, –·–.

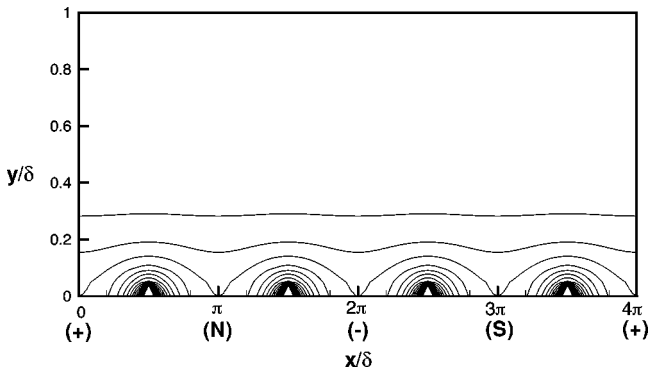


FIG. 14. Force distribution resulting from potential distribution representation in Fig. 13. Note that force is positive everywhere and contour values range from 2 to 40 [$N$] with 21 levels shown.

are the ones described above: namely, on conducting surfaces constant potential, and on nonconducting surfaces zero normal gradient of the potential functions.

After confirming the proper boundary conditions to use for calculating the Lorentz force, the realistic force was applied in a low Reynolds number turbulent channel flow. Figure 15 demonstrates that the realistic and ideal-force cases each achieve a similar amount of drag reduction with the same power consumption, validating the earlier idealized-force results. It was hoped that the peaks of force at the edges of the conductors would suppress the vortices in a more efficient manner than the idealized-force distribution. Although the realistic force also creates a substantial drag reduction, it is no more efficient at doing so than the idealized force is.

## VI. OPEN LOOP CONTROL: IDEALIZED SPATIALLY OSCILLATING LORENTZ FORCE

Alternating the polarity of the electrodes in time creates a temporally varying Lorentz force. We have shown above that there appears to be an optimal oscillation frequency that

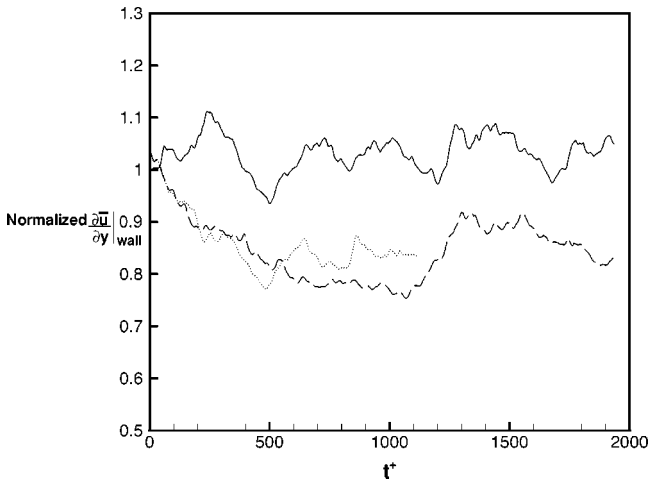


FIG. 15. The drag history comparison between realistic and ideal force distributions for $\mathrm{Re}_\tau=100$, $\Delta^+=10$, and $\mathrm{St}=10\pi$. No statistically significant difference can be discerned between the two cases: no control, —; realistic case, ···; ideal case, ---.

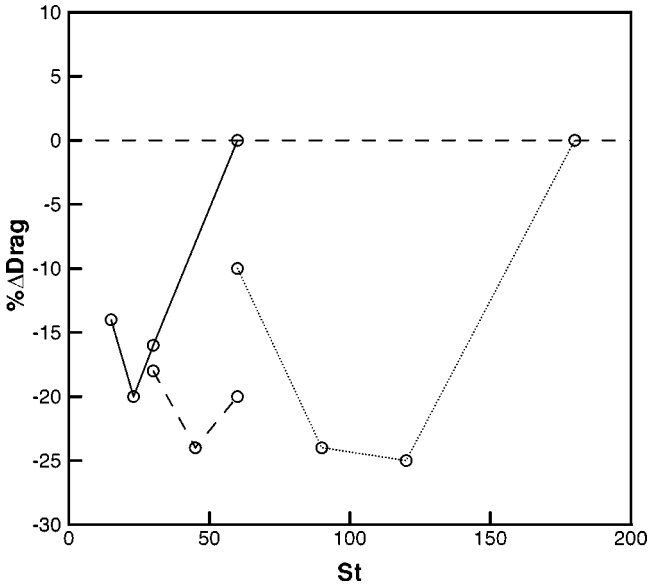


FIG. 16. Drag comparison for a spatially varying spanwise Lorentz force for $\lambda_x^+=300$, 600, 1200, $\Delta^+=10$ and $\mathrm{Re}_\tau=100$, illustrating that there is an optimal St for each streamwise wavelength: $\lambda_x^+=1200$, —; $\lambda_x^+=600$, ---; $\lambda_x^+=300$, ⋯.

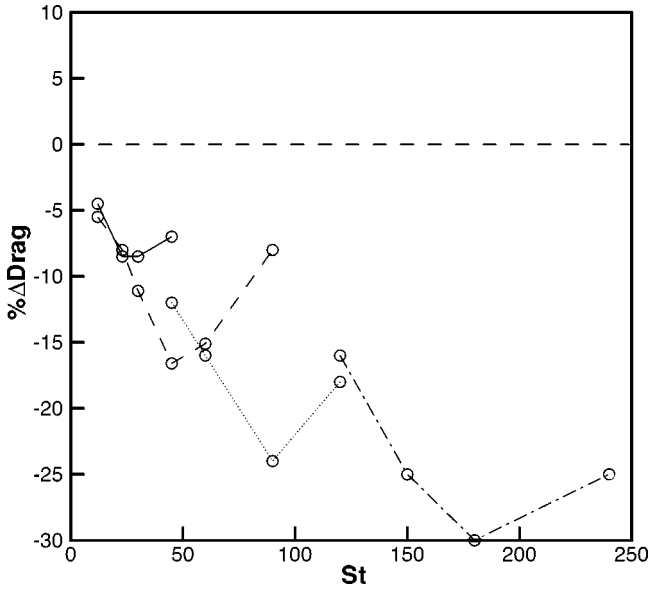


FIG. 17. Drag comparison for a spatially varying spanwise Lorentz force for $\lambda_x^+=300$, 600, 1200, 2400, $\Delta^+=10$ and $\mathrm{Re}_\tau=200$, again revealing that there is an optimal St for each streamwise wavelength. In addition, there appears to be an optimal wavelength for producing maximum drag reduction: $\lambda_x^+=2400$, —; $\lambda_x^+=1200$, ---; $\lambda_x^+=600$, –·–; $\lambda_x^+=300$, ⋯.

reduces drag by approximately 40% and whose magnitude in wall units, $T^+=50-100$, is consistent with the Akhavan *et al.*[12] results. Another approach can be taken. By altering the arrangement of the electrodes, the resulting force distribution can be made to oscillate spatially. This spatially oscillating force will appear to oscillate in time as eddies convect downstream. It is expected that it will be easier in practice to implement this control scheme if the same effect upon the turbulence can be obtained without having to alternate the polarity. Another idealized-force distribution is used to test the feasibility of the spatial-oscillation strategy. We impose a force given by

$$f_z^+=\mathrm{St}\exp\left(-\frac{y^+}{\Delta^+}\right)\sin\left(\frac{2\pi x^+}{\lambda_x^+}\right), \tag{35}$$

where $\lambda_x^+$ is the wavelength in the streamwise direction and again $\Delta^+=a^+/\pi$ is the penetration depth. This force distribution is applied to a turbulent channel flow with $\mathrm{Re}_\tau=100$ and 200.

For all cases, $\Delta^+$ was held fixed at a value of 10. A parametric study of the effect of Stuart number and wavelength, $\lambda_x^+$, was performed for both Reynolds numbers. Figures 16 and 17 illustrate that for fixed values of $\lambda_x^+$ there exists an optimal Stuart number in the sense it produces the greatest drag reduction and that appears to be inversely proportional to the wavelength. Approximately 30% maximum drag reduction is achieved using this type of spatial control. However, it can be seen from Figs. 16 and 17 that the required magnitude of St is still large and is of the same order as that of the temporally oscillating spanwise Lorentz force described in Sec. IV. Thus, this open-loop control scheme is not efficient either since the efficiency parameter $\eta$ is still much smaller than 1. The figures also reveal the existence of an optimal wavelength for producing the greatest amount of drag reduction, $\lambda_{x,\mathrm{opt}}^+\approx 300$, which is the same for both Reynolds numbers. The drag histories are presented in Figs. 18, 19, and 20 for $\lambda_x^+=600$, 300, and 150, respectively. Drag increases for all amplitudes when $\lambda_x^+=150$. Further consideration is given below to the spatial cases that correspond to equivalent temporal oscillation cases. The turbulent statistics (not presented here) of the spatially varying Lorentz force cases reveal the same trends that were observed for the temporally oscillating force.

To estimate the dependence of drag reduction on $\lambda_x^+$, a mean–momentum analysis similar to the one used to approximate the optimal temporal oscillation can be employed. Due to the force distribution shown in Eq. (35), the mean streamwise velocity, $U_{\mathrm{mean}}^+$, is assumed to be constant so that

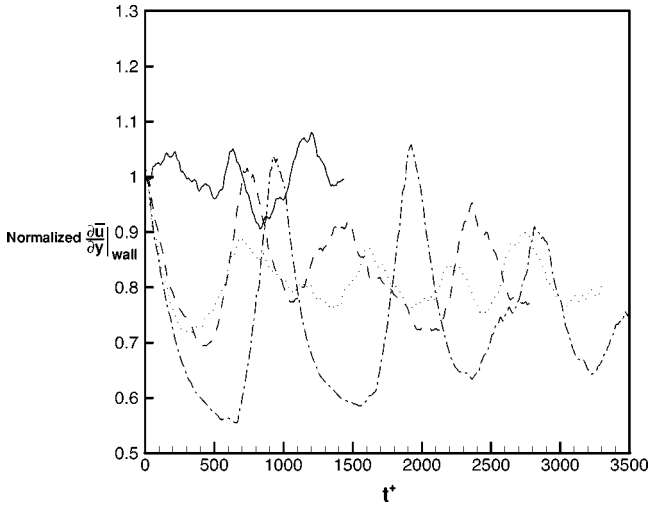


FIG. 18. Drag history for $\lambda_x^+=600$ and $\mathrm{Re}_\tau=100$ showing the existence of an optimal St: no control, —; St=30, ---; St=45, –·–; St=60, ⋯.

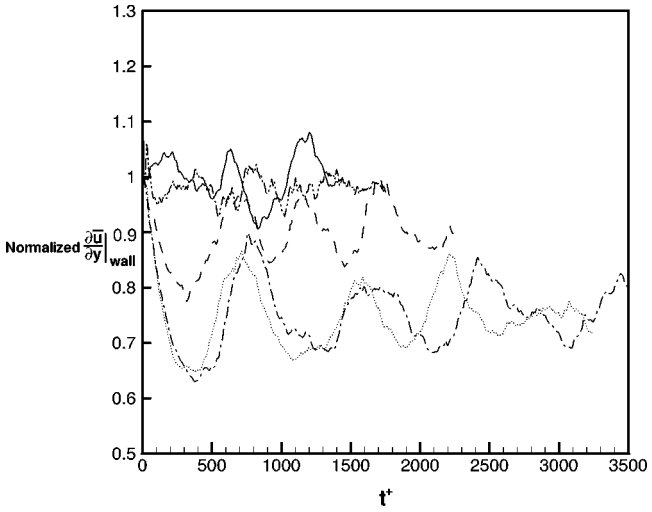


FIG. 19. Drag history for $\lambda_x^+=300$ and $\mathrm{Re}_\tau=100$ illustrating the existence of an optimal St: no control, —; St=60, ---; St=90, –·–; St=120, ···; St=180, –·–.

a closed form solution can be obtained for the mean spanwise velocity, $W^+$. The governing equation then becomes

$$U^+\frac{\partial W^+}{\partial x^+}=\frac{\partial^2 W^+}{\partial x^{+2}}+\frac{\partial^2 W^+}{\partial y^{+2}}+\frac{\mathrm{St}}{\mathrm{Re}_\tau}\exp\left(-\frac{y^+}{\Delta^+}\right)\sin(k_x^+x^+), \tag{36}$$

subject to

$$W^+(x^+,y^+=0)=0, \tag{37}$$

$$W^+(x^+,y^+\to\infty)=0. \tag{38}$$

Here, $k_x^+=2\pi/\lambda_x^+$ is the streamwise wave number and the boundary conditions are periodic in the streamwise direction. Since $k_x^+$ is fixed, no harmonics will appear in the solution. The form of the solution can be chosen as $f(y^+)\cos(k_x^+x^+)+g(y^+)\sin(k_x^+x^+)$. When this form is used, along with the condition $U^+/k_x^+\gg 1$ (since $k_x^+$ is finite and typically has a value several orders of magnitude less than $U^+$), the solution for $W^+(x^+,y^+)$ is found to be

$$W^+(x^+,y^+)=\frac{\mathrm{St}}{\mathrm{Re}_\tau k_x^+U^+}\left[\exp\left(-y^+\sqrt{\frac{k_x^+U^+}{2}}\right)\times\cos\left(y^+\sqrt{\frac{k_x^+U^+}{2}}-k_x^+x^+\right)-\exp\left(-\frac{y^+}{\Delta^+}\right)\cos(k_x^+x^+)\right]. \tag{39}$$

The maximum velocity near the wall is proportional to the magnitude of the forcing, as expected, but it also inversely depends on the mean velocity, the Reynolds number, and the streamwise wave number,

$$W^+_{\max}\propto\frac{\mathrm{St}}{\mathrm{Re}_\tau k_x^+U^+}. \tag{40}$$

Therefore, to influence the near-wall structures $W^+_{\max}$ must be above a certain threshold. Equation (40) implies that, for a fixed $\mathrm{Re}_\tau$, St is directly proportional to $k_x^+$, or $1/\lambda_x^+$, a result also indicated by the present DNS results. However, for a fixed $k_x^+$, St is proportional to $\mathrm{Re}_\tau$. Plots of Eq. (39) and the mean spanwise velocity induced by the spatially oscillating force in the turbulent channel flow case for $\mathrm{Re}_\tau=100$ are shown in Fig. 21. Even though Eq. (36) assumes that the mean streamwise velocity is constant with distance from the wall, which is not the case, it can be seen that the two plots are very similar to each other. This similarity supports the scaling relations following from Eq. (39).

An optimal range of $\lambda_x^+$ can now be estimated. If the variation of the induced spanwise velocity with streamwise direction is negligible compared to the variation in the wall–normal direction (which is the case), the equation for $W^+(x^+,y^+)$ [Eq. (39)] becomes identical to the temporally evolving solution Eq. (31), with $x^+$ and $\lambda_x^+$ replaced by $U^+t^+$ and $U^+T^+$, respectively. This suggests that the arguments used to estimate the optimal range for $T^+$ can be applied here as well. With $25\leqslant T^+_{\mathrm{opt}}\leqslant 125$ and $U^+\approx 10$ (the mean streamwise velocity at the $y^+=25$ location of the average center of the streamwise vortices), the optimal range for $\lambda_x^+$ is $250\leqslant\lambda^+_{x,\mathrm{opt}}=U^+T^+_{\mathrm{opt}}\leqslant 1250$. This range is consistent with the DNS simulations (see Figs. 16–20).

Also, from the DNS simulations for $\mathrm{Re}_\tau=100$ and 200, and normalizing by $\pi$ (Figs. 16 and 17 and with $U^+\approx 10$ for both $\mathrm{Re}_\tau$),

$$\left(\frac{\mathrm{St}\,\lambda_x^+}{\mathrm{Re}_\tau U^+\pi}\right)_{\mathrm{opt}}\approx 10. \tag{41}$$

Figure 22 confirms this result. Comparing with the results for a temporally oscillating spanwise Lorentz force, $(\mathrm{St}\,T^+/\mathrm{Re}_\tau\pi)_{\mathrm{opt}}=20$ (assuming $T^+_{\mathrm{opt}}=\lambda^+_{x,\mathrm{opt}}/U^+$), it can be seen that the optimal St for this spatially oscillating body force is half of that found for the temporally oscillating force. Considering that the attained drag reductions are almost the same, it is concluded that a spatially oscillating Lorentz force is twice as efficient as a temporally oscillating

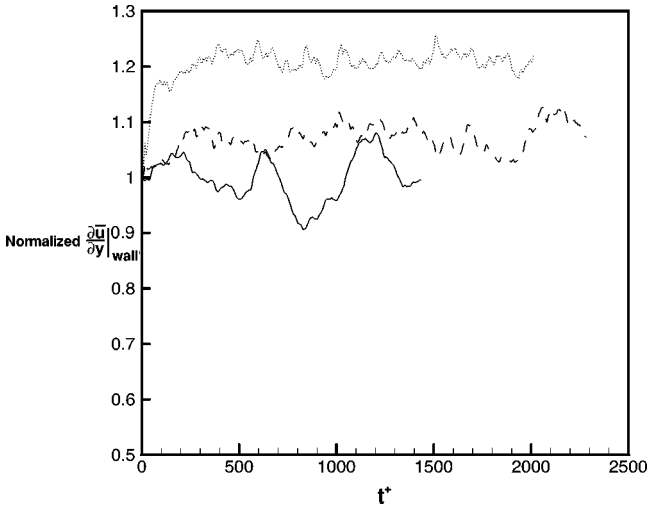


FIG. 20. Drag history for $\lambda_x^+=150$ and $\mathrm{Re}_\tau=100$ revealing that drag increase occurs for all amplitudes: no control, —; St=120, ---; St=240, ···.

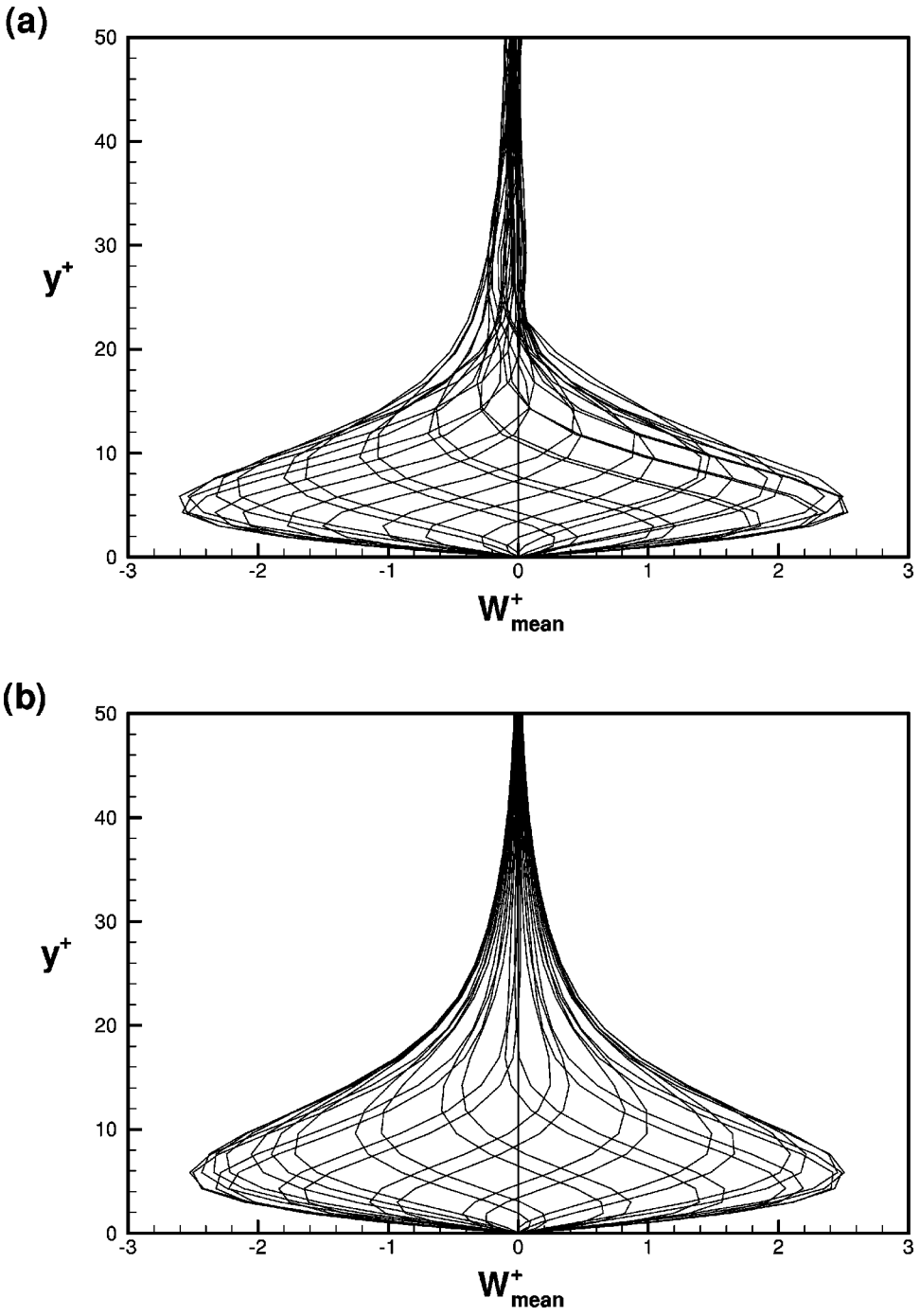


FIG. 21. Induced spanwise velocity profiles: (a) turbulent case; (b) analytical solution of Eq. (36). The different curves represent different instances in time during the forcing period.

Lorentz force. The efficiency, however, does not improve since $\eta$ is several orders of magnitude less than 1.

## VII. IDEALIZED CLOSED-LOOP CONTROL

The open-loop spanwise oscillating force control scheme was found above to be inefficient in regards to the ratio of power saved to power consumed. Based on the work reported by Choi *et al.*[17] and Lee *et al.*,[23,24] a closed-loop control scheme using an idealized wall–normal Lorentz force was examined to test whether or not such a scheme would be more efficient.

By turning the electrodes and magnets perpendicular to one another (Fig. 23), a significant wall–normal force can be created. Nosenchuck and Brown[7] proposed such a configuration to produce a significant wall–normal force and reported that the local wall-shear stresses in the control region were reduced by approximately 90%. Choi *et al.*[17] showed that by placing detection planes in the flow at certain locations away from the wall, the near-wall events (i.e., sweeps and ejections) associated with the turbulence structures responsible for high skin friction can be identified. They showed that approximately 25% drag reduction can be attained by using surface blowing and suction that are equal and opposite to the wall–normal component of velocity at $y^+ = 10$. However, it is difficult in practice to detect flow variables within the flow field itself. In an attempt to allevi-

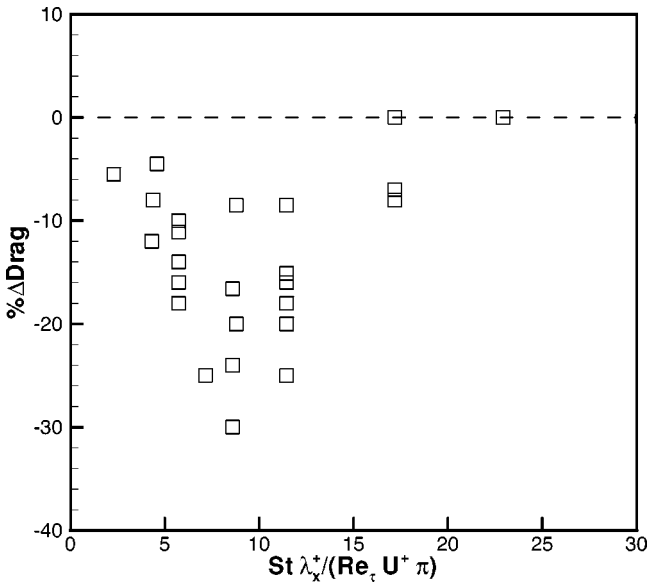


FIG. 22. Magnitude of Eq. (41), $\mathrm{St}\,\lambda_x^+/(\mathrm{Re}_\tau U^+\pi)$, compared to percent drag reduction for $\Delta^+=10$. It can be seen that a value of approximately 10 is most effective at reducing the drag.

ate this difficulty, Lee *et al.*[23] used a neural network to find that an optimal blowing/suction pattern based on weighted values of the local spanwise shear at the wall, $\partial w/\partial y|_{\mathrm{wall}}$, leads to approximately 20% reduction. Lee *et al.*[24] used suboptimal control theory to find an optimal blowing and suction pattern, leading to approximately a 20% reduction in skin-friction drag. They found the optimal actuation to be proportional to the spanwise gradient of the spanwise shear at the wall, $\partial/\partial z(\partial w/\partial y)|_{\mathrm{wall}}$. Thus, wall transpiration control that utilizes $v_{\mathrm{wall}}\sim\partial/\partial z(\partial w/\partial y)|_{\mathrm{wall}}$ can produce significant drag reduction with a relatively small required input. Other researchers have shown similar success by using different types of opposition feedback control schemes in order to counteract the near-wall turbulence events. For example, Koumoutsakos[25] has shown that drag can be significantly reduced by a feedback control algorithm through manipulation of the vorticity flux components at the wall. It was found that 40% drag reduction could be accomplished using wall transpiration corresponding to roughly 5%–15% of the bulk velocity. Also, Bewley and Moin[26] discussed using both wall

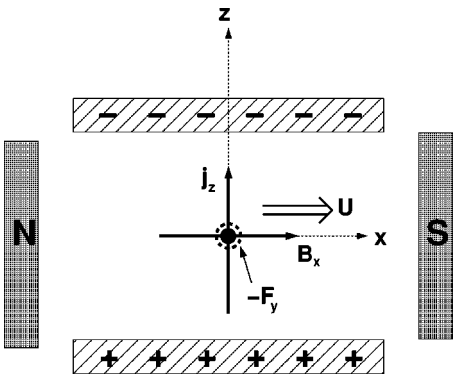


FIG. 23. Electrode and magnet configuration that produces a significant wall–normal force (Nosenchuck and Brown[7]).

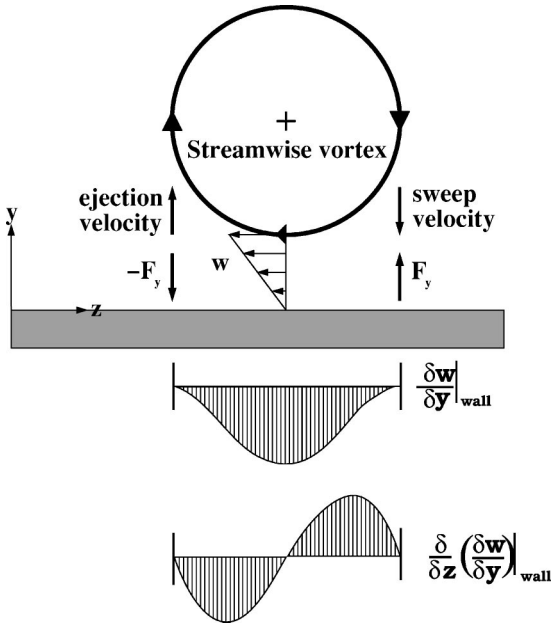


FIG. 24. Control scheme to detect and suppress near-wall streamwise vortices (Choi *et al.*[17]). Both the spanwise shear stress profile and corresponding spanwise shear stress gradient at the wall are shown.

transpiration and the Lorentz force as means to reduce the drag and wall pressure fluctuations in a channel geometry through a feedback control scheme using optimal control theory. It was found that 17% drag reduction could be accomplished by wall transpiration at low control input levels while a formulation for reducing the wall pressure fluctuations using the Lorentz force was proposed.

Figure 24 shows the principle behind the two control schemes derived by Lee *et al.*[23,24] The presence of a streamwise vortex above the wall produces a spanwise shear, whose spanwise distribution at the wall is shown in the figure. The spanwise gradient of the spanwise shear at the wall has a distribution that acts in opposition to the sweep and ejection events associated with the vortex. By using this distribution as a pattern for blowing and suction and modifying its magnitude, Lee *et al.*[23,24] successfully demonstrated that the interaction between the vortex and the wall can be minimized, leading to a reduction in skin-friction drag.

As an analogy to the methods described above, an idealized wall–normal force distribution was applied to a low Reynolds number turbulent channel flow ($\mathrm{Re}_\tau=100$). The objective of this scheme is to locate and manipulate the near-wall turbulent structures responsible for high-skin friction, namely, the streamwise vortices.

Two methods of closed-loop control are used to adjust the magnitude of this force at the wall: (1) weighted values of $\partial w/\partial y|_{\mathrm{wall}}$, where the weights are determined by previous work using a neural network;[23] (2) direct calculation of $(1/|k_z|)ik_z(\widehat{\partial w/\partial y}|_{\mathrm{wall}})$, where the ''hat'' symbol denotes the Fourier coefficient, $k_z$ is the spanwise wave number, and the $1/|k_z|$ factor was determined to be necessary from suboptimal control theory.[24] The force distribution was chosen to exponentially decay in the wall–normal direction in the same manner as the open-loop spanwise force control scheme and

TABLE III. Cases studied using seven point weight method and direct method.

| Method | $\Delta^+$ | $\mathrm{St}\|_{\mathrm{rms}}$ |
|---|---|---|
| Seven point only | 10 | 1 |
| | | 2 |
| | | 4 |
| Seven point and direct | 5 | 4 |
| | 10 | |
| | 15 | |

its magnitude, $f_y^+$, is chosen to be proportional to $\partial/\partial z(\partial w/\partial y|_{\mathrm{wall}})$,

$$f_y^+ = \mathrm{St}(x,z)\exp\left(-\frac{y^+}{\Delta^+}\right). \tag{42}$$

Note that this wall–normal Lorentz force is idealized in the sense that all realizable forces should be three dimensional.

For the first method, the $\partial w/\partial y|_{\mathrm{wall}}$ weights, $\mathcal{W}_j$, were determined from a neural network, which found the optimal values. In other words, seven points in the spanwise direction were used, with values of $(-\frac{1}{3},0,-1,0,1,0,\frac{1}{3})$, or $\mathcal{W}_j=[1-(-1)^j]/[2j]$. We denote this case as the ''seven-point method,'' and $\mathrm{St}(x,z)$ is calculated by

$$\mathrm{St}(x_k,z_l) = C\sum_{j=-3}^{3}\mathcal{W}_j\left.\frac{\partial w}{\partial y}\right|_{k,l+j}, \tag{43}$$

where $C$ is chosen such that the resulting $\mathrm{St}|_{\mathrm{rms}}$ matches a predetermined value.

The second method, referred to hereafter as the ''direct method,'' involves calculating $(1/|k_z|)ik_z(\partial w/\partial y)|_{\mathrm{wall}}$. This quantity, as shown in Fig. 24, represents a force counteracting the sweep and ejection motions. The value of $\widehat{\mathrm{St}}(k_x,k_z)$ is given as

$$\widehat{\mathrm{St}}(k_x,k_z) = C\frac{ik_z}{|k_z|}\left.\widehat{\left(\frac{\partial w}{\partial y}\right)}\right|_{\mathrm{wall}}, \tag{44}$$

with $C$ again being chosen such that the resulting $St|_{\mathrm{rms}}$ matches a specified value.

Five test cases were examined for both control schemes in a low Reynolds number ($\mathrm{Re}_\tau=100$) turbulent channel flow. Table III lists the parameters used for these cases. Three values for $\mathrm{St}|_{\mathrm{rms}}$ were chosen for the seven-point method: 1, 2, and 4. Only $\mathrm{St}|_{\mathrm{rms}}=4$ was used for the direct method, for comparison with the weighted approach; however, three different decay parameters were chosen to test where the forcing should be positioned in order to have the greatest effect on the near-wall turbulent motions. For both methods, it was found that a wall forcing of $\mathrm{St}|_{\mathrm{rms}}=4$ with $\Delta^+=10$ gave the best result and it was as successful in reducing drag as was the spanwise-temporal-oscillating force with $f_z^+|_{\mathrm{wall}}=20\pi$ (Fig. 25), yielding a $P^*_{\mathrm{saved}}$ to $P^*_{\mathrm{used}}$ ratio of approximately 0.167 (i.e., $\eta=0.167$), in contrast to the spanwise-temporal-oscillating-case ratio of $10^{-3}$. The other two values of $\Delta^+$, 5, and 15 with $\mathrm{St}|_{\mathrm{rms}}=4$, either did not demonstrate significant drag reduction ($\Delta^+=5$) or reduced the drag the same amount as $\Delta^+=10$ ($\Delta^+=15$). Therefore, the results from these two cases are not shown here.

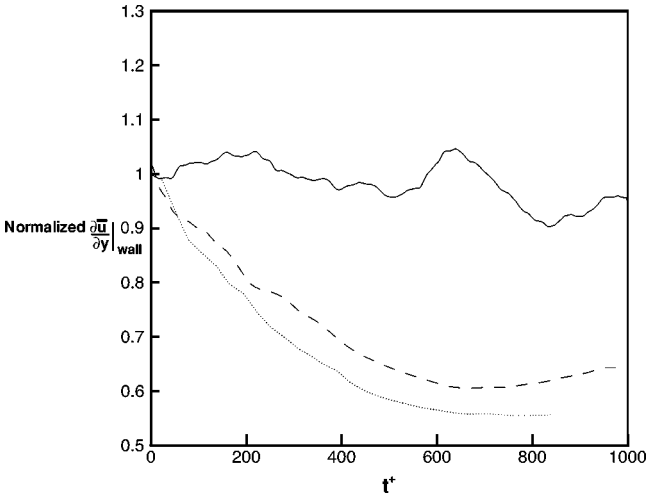


FIG. 25. Drag history comparison between no control and seven-point weight and direct closed-loop control methods, both having $\mathrm{St}|_{\mathrm{rms}}=4$: no control, —; seven-point control, ---; direct method, ⋯.

Thus, closed-loop control schemes require much less power input. However, the drawback to these two methods is that the spanwise wall-shear stress needs to be measured. Furthermore, a real force generated from a tile configuration will be three dimensional, and the effect of these additional forces needs to be investigated.

## VIII. CONCLUSIONS

Our purpose in this paper is to examine effective means of reducing the skin-friction drag by utilizing the Lorentz force in a turbulent boundary layer. We start with the premise that an effective way to reduce the drag is to disturb the semiequilibrium state between the near-wall streamwise vortices and the wall. It is shown that the Lorentz force applied perpendicularly to these vortices can cause a substantial skin-friction decrease.

Several methods are found to diminish the drag, but at a great cost of input power. It is demonstrated that a Lorentz force produced by strips of magnets and electrodes with a reasonable magnetic field strength and applied voltage ($B_0=0.35-0.4\,\mathrm{T}$ and $V=4-100\,\mathrm{V}$)[4,8] can create sufficient perturbations parallel to the wall and perpendicular to the near-wall streamwise vortices such that the skin-friction drag is reduced by approximately 40%. Consideration of the power required to generate this type of Lorentz force reveals that the present configuration of alternating strips of magnets and electrodes is not practical. As a result, different strategies to create a more efficient Lorentz force are examined.

A spatially oscillating spanwise force distribution is investigated to take advantage of the convection of streamwise vortices in the downstream direction. This type of spatial oscillation is easier to implement in practice, since it requires no oscillation in time of the force field. It is found that a significant drag reduction is attained; however, the required forcing at the wall is large, leading to the conclusion that the

inefficiency of this control scheme is of the same order of magnitude as that for the temporal oscillating cases.

Two similar idealized closed-loop control schemes are tested that detect the presence of turbulence structures near the control wall, and that apply a countermeasure to mitigate their interaction with the wall with an idealized wall–normal Lorentz force. This approach produces as much drag reduction as the spanwise oscillating force does, but with a much lower required force at the wall. Thus, these two schemes are found to be the most efficient of those considered. The only drawback of these two methods is that the local spanwise shear stress needs to be measured at the wall.

Finally, it is worthwhile to mention the relevance of our results to those from the tile experiments of Nosenchuck and Brown[7,8] and Bandyopadhyay and Castano.[9] The scales of each of their tiles are on the order of 1000 wall units, thus implying that their Lorentz forces also affect the outer-layer structures. It can be shown that the three-dimensional force field created by these tiles produces wall–parallel components that are much stronger than the wall–normal component in the near-wall region. Furthermore, depending on the tile arrangement, the spanwise force component can be caused to change sign in the streamwise direction. This result suggests that an oscillating spanwise force in the near-wall region may play an effective role in reducing skin-friction drag. This conjecture, however, needs to be investigated further.

## ACKNOWLEDGMENTS

We are grateful to Dr. Gary N. Coleman and Professor H. Choi for many helpful discussions throughout the course of this work. All numerical simulations were carried out on the supercomputing facilities at SDSC, NASA Ames Research Center (NAS) and DoD ASC-MSRC. Financial support was provided by ONR. In addition, ANSYS support was provided by the UCLA Fusion Research Group and Collaborative Solutions Incorporated, Carlsbad, CA. All support is gratefully acknowledged.

## APPENDIX: ANALYSIS OF A SIMPLIFIED LORENTZ FORCE PRODUCED BY AN ALTERNATING ARRAY OF ELECTRODES AND MAGNETS

From Sec. II, the dimensional form of the governing equations for both the magnetic flux density vector, **B**, and electric potential, $\phi$, functions are governed by Laplace's equation,

$$\nabla^2\phi=0, \tag{A1}$$

$$\nabla^2\mathbf{B}=0, \tag{A2}$$

with

$$\mathbf{J}=-\sigma\nabla\phi. \tag{A3}$$

It is assumed that the current and magnetic flux density distributions are sinusoidal to simplify the solution and to provide a spanwise force that does not vary with the streamwise coordinate, $x$. We also assume $B_z=0$ and neglect the induced magnetic field. Neumann boundary conditions for $\phi$ and Dirichlet boundary conditions for **B** are imposed at the surface of the array. The wall values at $y=0$ are thus

$$J_y|_{\text{wall}}=J_0\sin\left(\frac{\pi}{2a}x\right)=-\sigma\left.\frac{\partial\phi}{\partial y}\right|_{\text{wall}}, \tag{A4}$$

$$B_y|_{\text{wall}}=B_0\cos\left(\frac{\pi}{2a}x\right). \tag{A5}$$

The domain for solving Eqs. (A1)–(A3) is a channel with height $2\delta$ and the upper wall is nonconducting (i.e., $B_{y=2\delta}|_{\text{wall}}=0$ and $J_{y=2\delta}|_{\text{wall}}=0$). The current density and magnetic flux density distributions become

$$J_x(x,y)=-\frac{J_0}{\tanh\left(\frac{\pi}{a}\delta\right)}\cos\left(\frac{\pi}{2a}x\right)\left[\cosh\left(\frac{\pi}{2a}y\right)-\tanh\left(\frac{\pi}{a}\delta\right)\sinh\left(\frac{\pi}{2a}y\right)\right], \tag{A6}$$

$$J_y(x,y)=-\frac{J_0}{\tanh\left(\frac{\pi}{a}\delta\right)}\sin\left(\frac{\pi}{2a}x\right)\left[\sinh\left(\frac{\pi}{2a}y\right)-\tanh\left(\frac{\pi}{a}\delta\right)\cosh\left(\frac{\pi}{2a}y\right)\right], \tag{A7}$$

$$B_x(x,y)=-B_0\sin\left(\frac{\pi}{2a}x\right)\left[\sinh\left(\frac{\pi}{2a}y\right)-\frac{\cosh\left(\frac{\pi}{2a}y\right)}{\tanh\left(\frac{\pi}{a}\delta\right)}\right], \tag{A8}$$

$$B_y(x,y)=B_0\cos\left(\frac{2\pi}{a}x\right)\left[\cosh\left(\frac{\pi}{2a}y\right)-\frac{\sinh\left(\frac{\pi}{2a}y\right)}{\tanh\left(\frac{\pi}{a}\delta\right)}\right]. \tag{A9}$$

By taking the vector product of the current density and the magnetic flux density, the resulting force distribution acts only in the spanwise direction and is only a function of the wall–normal distance, $y$,

$$f_z=J_0B_0\left[\sinh\left(\frac{\pi}{2a}y\right)-\frac{\cosh\left(\frac{\pi}{2a}y\right)}{\tanh\left(\frac{\pi}{a}\delta\right)}\right]\times\left[\cosh\left(\frac{\pi}{2a}y\right)-\frac{\sinh\left(\frac{\pi}{2a}y\right)}{\tanh\left(\frac{\pi}{a}\delta\right)}\right]. \tag{A10}$$

When $\delta/a\to\infty$,

$$f_i = \delta_{i3} J_0 B_0 \exp\left( -\frac{\pi}{a} y \right). \tag{A11}$$


[1] A. B. Tsinober, ''MHD drag reduction,'' in *Viscous Drag Reduction in Boundary Layers*, Vol. 123 of Progress in Astronautics and Aeronautics, edited by D. M. Bushnell and J. N. Hefner (American Institute of Aeronautical and Astronautics, Washington D.C., 1989), pp. 327–349.

[2] A. K. Gailitis and O. A. Lielausis, ''On the possibility of drag reduction of a flat plate in an electrolyte,'' Appl. Magnetohydrodyn. Trudy Inst. Fisiky AN Latvia SSR **12**, 143 (1961).

[3] A. B. Tsinober and A. G. Shtern, ''Possibility of increasing the flow stability in a boundary layer by means of crossed electric and magnetic fields,'' Magnetohydrodynamics **3**, 152 (1967).

[4] C. Henoch and J. Stace, ''Experimental investigation of a salt water turbulent boundary layer modified by an applied streamwise magnethydrodynamic body force,'' Phys. Fluids **7**, 1371 (1995).

[5] C. H. Crawford and G. E. Karniadakis, ''Reynolds stress analysis of EMHD-controlled wall turbulence. Part I,'' Phys. Fluids **9**, 788 (1997).

[6] C. C. Lin, *The Theory of Hydrodynamic Stability* (Cambridge University Press, Cambridge, 1966).

[7] D. M. Nosenchuck and G. L. Brown, ''Discrete spatial control of wall shear stress in a turbulent boundary layer,'' in *Near-Wall Turbulent Flows*, edited by R. M. C. So, C. G. Speziale, and B. E. Launder (Elsevier Science Publishers B.V., New York, 1993), pp. 689–698.

[8] D. M. Nosenchuck, ''Spatial and temporal characteristics of boundary layers controlled with the Lorentz force,'' in *12th Australasian Fluid Mechanics Conference* (University of Sydney Press, Sydney, Australia, 1995), pp. 93–96.

[9] P. R. Bandyopadhyay and J. M. Castano, ''Micro-tiles for electromagnetic turbulence control in saltwater—preliminary investigations,'' in *Proceedings of the Forum on Control of Transitional and Turbulent Flows, Fluids Engineering Division Conference*, ASME, 7–11 July 1996, edited by D. E. Parkh and R. K. Agarwal (ASME, San Diego, 1996), Vol. FED-Vol. 237, pp. 53–60.

[10] P. L. O'Sullivan and S. Biringen, ''Direct simulations of low Reynolds number turbulent channel flow with emhd control,'' *28th AIAA Fluid Dynamics Conference, 4th AIAA Shear Flow Control Conference*, 29 June–2 July 1997, pp. 1–13.

[11] This amount of skin-friction drag reduction appears too small to be statistically significant but the authors contend that the trend is important and correct.

[12] R. Akhavan, W. J. Jung, and N. Mangiavacchi, ''Turbulence control in wall-bounded flows by spanwise oscillations,'' in *Applied Scientific Research*, Vol. 51 of *Advances in Turbulence IV*, edited by F. T. M Nieuwstadt (Kluwer, New York, 1993), pp. 299–303.

[13] F. Laadhari, L. Skandaji, and R. Morel, ''Turbulence reduction in a boundary layer by a local spanwise oscillating surface,'' Phys. Fluids **6**, 3218 (1994).

[14] P. Bradshaw and N. S. Pontikos, ''Measurements in the turbulent boundary layer on an 'infinite' swept wing,'' J. Fluid Mech. **159**, 105 (1985).

[15] G. N. Coleman, J. Kim, and A. Le, ''A numerical study of three-dimensional wall-bounded flows,'' Int. J. Heat Fluid Flow **19**, 333 (1996).

[16] O. Sendstad and P. Moin, ''The near-wall mechanics of three-dimensional turbulent boundary layers,'' Report No. TF-57, Thermosciences Division, Department of Mechanical Engineering, Stanford University, Stanford, CA, 1992.

[17] H. Choi, P. Moin, and J. Kim, ''Active turbulence control for drag reduction in wall-bounded flows,'' J. Fluid Mech. **262**, 75 (1994).

[18] H. Choi, P. Moin, and J. Kim, ''Direct numerical simulation of turbulent flow over riblets,'' J. Fluid Mech. **255**, 503 (1993).

[19] J. Kim, P. Moin, and R. Moser, ''Turbulence statistics in a fully developed channel flow at low Reynolds number,'' J. Fluid Mech. **177**, 133 (1987).

[20] A. T. Le, G. N. Coleman, and J. Kim, ''Near-wall turbulence structures in three-dimensional boundary layers,'' in *Proceedings of the 1st International Symposium on Turbulence and Shear Flow Phenomena*, September 1999, Santa Barbara, CA, 1999.

[21] The mean shear created near the wall is subject to a shear instability if the shear is maintained long enough to allow the instability to grow, such as the $T^+ = 500$ case. When $T^+ = 100$, however, the shear changes sign quickly enough to prevent such an instability.

[22] ANSYS, ANSYS *Reference Manual*, Swanson Analysis Systems, Inc., Houston, PA, December 1992, Version 5.0.

[23] C. Lee, J. Kim, D. Babcock, and R. Goodman, ''Application of neural networks to turbulence control for drag reduction,'' Phys. Fluids **9**, 1740 (1997).

[24] C. Lee, J. Kim, and H. Choi, ''Suboptimal control of turbulent channel flow for drag reduction'' J. Fluid Mech. **358**, 245 (1998).

[25] P. Koumoutsakos, ''Vorticity flux control for a turbulent channel flow,'' Phys. Fluids **11**, 248 (1999).

[26] T. Bewley and P. Moin, ''Optimal control of turbulent channel flows,'' *Active Control of Vibration and Noise*, ASME, 1994 (ASME, Chicago, 1994), Vol. DE-Vol. 75, pp. 221–227.